
Research Articles: Cellular/Molecular

Target cell type-dependent differences in Ca²⁺ channel function underlie distinct release probabilities at hippocampal glutamatergic terminals

Tímea Éltes^{1,2,#}, Tekla Kirizs^{1,2,#}, Zoltan Nusser¹ and Noemi Holderith¹

¹Laboratory of Cellular Neurophysiology, Institute of Experimental Medicine, Hungarian Academy of Sciences, 1083 Budapest, HUNGARY

²János Szentágothai School of Neurosciences, Semmelweis University, Budapest H1085, Hungary

DOI: 10.1523/JNEUROSCI.2024-16.2017

Received: 24 June 2016

Revised: 4 January 2017

Accepted: 10 January 2017

Published: 23 January 2017

Author contributions: T.E., T.K., and N.H. performed research; T.E., T.K., Z.N., and N.H. analyzed data; Z.N. and N.H. designed research; Z.N. and N.H. wrote the paper.

ZN is the recipient of a Hungarian Academy of Sciences Momentum Grant (Lendület, LP2012-29) and a European Research Council Advanced Grant (293681). N.H. is funded by Janos Bolyai Scholarships of the Hungarian Academy of Sciences. The financial support from these funding bodies is gratefully acknowledged. We would like to thank Éva Dobai and Dóra Rónaszéki for their excellent technical assistance, Borbála Bolonyai for contributing to the quantification of Elfn1/2-mGluR1# colocalization and NeuroLucida reconstructions, Miklós Szoboszlai for writing the gold distribution analysis software, Csaba Cserép for his invaluable help in EM tomography, Drs Balazs Hangya, Judit Makara and Gabor Makara for their help in statistical analysis, Dr Mark Eyre for his comments on the MS.

[#]Equal contribution

Correspondence: Zoltan Nusser (nusser@koki.hu) or Noemi Holderith (noemi.holderith@koki.mta.hu)

Cite as: J. Neurosci ; 10.1523/JNEUROSCI.2024-16.2017

Alerts: Sign up at www.jneurosci.org/cgi/alerts to receive customized email alerts when the fully formatted version of this article is published.

Accepted manuscripts are peer-reviewed but have not been through the copyediting, formatting, or proofreading process.

Copyright © 2017 the authors

1

2 **Target cell type-dependent differences in Ca²⁺ channel function underlie distinct release**
3 **probabilities at hippocampal glutamatergic terminals**

4

5

6 Tímea Éltes^{1,2#}, Tekla Kirizs^{1,2#}, Zoltan Nusser^{1*} and Noemi Holderith^{1*}

7

8 ¹Laboratory of Cellular Neurophysiology, Institute of Experimental Medicine, Hungarian
9 Academy of Sciences, 1083 Budapest, HUNGARY

10 ²János Szentágothai School of Neurosciences, Semmelweis University, Budapest H1085,
11 Hungary

12

13 [#] Equal contribution

14 Short title: Target cell type-dependent differences in presynaptic Ca²⁺ channel function

15 No. of words in the Abstract: 159; Introduction: 583; Discussion: 1518

16 No. of pages: 40

17 No. of figures: 7

18 No. of tables: 1

19

20 Correspondence to: Zoltan Nusser (nusser@koki.hu) or
21 Noemi Holderith (noemi.holderith@koki.mta.hu)

22

23 **Acknowledgements**

24 ZN is the recipient of a Hungarian Academy of Sciences Momentum Grant (Lendület, LP2012-29)
25 and a European Research Council Advanced Grant (293681). N.H. is funded by Janos Bolyai
26 Scholarships of the Hungarian Academy of Sciences. The financial support from these funding
27 bodies is gratefully acknowledged. We would like to thank Éva Dobai and Dóra Rónaszéki for
28 their excellent technical assistance, Borbála Bolonyai for contributing to the quantification of
29 Elfn1/2-mGluR1 α colocalization and NeuroLucida reconstructions, Miklós Szoboszlay for writing
30 the gold distribution analysis software, Csaba Cserép for his invaluable help in EM tomography,
31 Drs Balazs Hangya, Judit Makara and Gabor Makara for their help in statistical analysis, Dr Mark
32 Eyre for his comments on the MS.

33 **ABSTRACT**

34 Target cell type-dependent differences in presynaptic release probability (P_r) and short-term
35 plasticity are intriguing features of cortical microcircuits that increase the computational
36 power of neuronal networks. Here we tested the hypothesis that different voltage-gated Ca^{2+}
37 channel densities in presynaptic active zones (AZs) underlie different P_r . Two-photon Ca^{2+}
38 imaging, triple immunofluorescent labeling and three-dimensional electron microscopic (EM)
39 reconstruction of rat CA3 pyramidal cell axon terminals revealed approximately 1.7 – 1.9-
40 times higher Ca^{2+} inflow per AZ area in high P_r boutons synapsing onto parvalbumin positive
41 interneurons than in low P_r boutons synapsing onto mGluR1 α positive interneurons. EM
42 replica immunogold labeling, however, demonstrated only 1.15-times larger Cav2.1 and
43 Cav2.2 subunit densities in high P_r AZs. Our results indicate target cell type-specific
44 modulation of voltage-gated Ca^{2+} channel function or different subunit composition as
45 possible mechanisms underlying the functional differences. In addition, high P_r synapses are
46 also characterized by a higher density of docked vesicles, suggesting that a concerted action of
47 these mechanisms underlies the functional differences.

48

49 **Significance Statement**

50 Target cell type-dependent variability in presynaptic properties is an intriguing feature of
51 cortical synapses. When a single cortical pyramidal cell establishes a synapse onto a
52 somatostatin-expressing interneuron (IN), the synapse releases glutamate with low
53 probability, whereas the next bouton of the same axon has high release probability when its
54 postsynaptic target is a parvalbumin-expressing IN. Here we used combined molecular,
55 imaging and anatomical approaches to investigate the mechanisms underlying these
56 differences. Our functional experiments implied a ~2-fold larger Ca^{2+} channel density in high

57 release probability boutons whereas freeze-fracture immunolocalization demonstrated only a
58 15% difference in Ca^{2+} channel subunit densities. Our results point toward a postsynaptic
59 target cell type-dependent regulation of Ca^{2+} channel function or different subunit
60 composition as the underlying mechanism.

61

62 **Introduction**

63 Target cell type-dependent differences in the probability of glutamate release (P_r) and the
64 consequent differences in short-term plasticity are well-established phenomena of cortical
65 microcircuits. Two decades ago, Thomson (1997) reported that neocortical pyramidal cell
66 (PC) to PC connections showed paired-pulse depression, whereas PC to certain interneuron
67 (IN) synapses displayed robust short-term facilitation. Later, a similar phenomenon was found
68 in the hippocampus (Ali et al., 1998; Ali and Thomson, 1998; Scanziani et al., 1998;
69 Losonczy et al., 2002), where combined functional and molecular neuroanatomical
70 approaches led to the identification of the postsynaptic IN types. Somatostatin and
71 metabotropic glutamate receptor 1α - (mGluR1 α) expressing, oriens-lacunosum moleculare
72 (O-LM) and oriens-bistratified (O-Bi) INs of the CA1 area receive facilitating EPSCs with
73 low initial P_r , whereas synaptic inputs onto fast-spiking (FS) parvalbumin- (PV) expressing
74 INs (e.g. basket, axo-axonic, bistratified cells) display short-term depression and have high
75 initial P_r (Atwood and Karunanithi, 2002; Losonczy et al., 2002; Biro et al., 2005; Koester and
76 Johnston, 2005; Mercer et al., 2012). Simultaneous recordings between a presynaptic PC and
77 two distinct types of IN revealed that the axon of a single PC can transmit different aspects of
78 information coded in a complex spike train to distinct postsynaptic cell types (Markram et al.,
79 1998b, 1998a; Reyes et al., 1998; Pouille and Scanziani, 2004; Koester and Johnston, 2005).
80 It has also been demonstrated that distinct types of short-term plasticity enable neuronal

81 networks to perform complex computations (Pouille and Scanziani, 2004), but almost nothing
82 is known about the mechanisms underlying these functional differences.

83 A candidate protein bestowing different P_r and short-term plasticity to axon terminals was
84 mGluR7, a metabotropic glutamate receptor that shows postsynaptic target cell type-
85 dependent differences in its presynaptic density (Shigemoto et al., 1996). However, a group
86 III mGluR-specific antagonist failed to abolish the differences in short-term plasticity of
87 synapses expressing or lacking mGluR7 (Losonczy et al., 2003). More recently, Sylwestrak
88 and Ghosh (2012) identified the extracellular leucine-rich repeat fibronectin containing
89 protein 1 (Elfn1) as a key molecule in bestowing short-term facilitation. This protein is
90 selectively expressed postsynaptically in O-LM cell somata and dendrites, and imposes
91 facilitating neurotransmitter release to the presynaptic axon terminals. Although, to date, there
92 is no data available regarding the mechanisms underlying the low initial P_r of these facilitating
93 synapses, Rozov et al. (2001) put forward an elegant hypothesis based on their experiments
94 involving fast and slow Ca^{2+} buffers. They postulated that the low initial P_r of facilitating
95 cortical PC synapses can be explained by a larger coupling distance between voltage-gated
96 Ca^{2+} channels and Ca^{2+} sensors on the docked vesicles compared to the high P_r PC synapses
97 on FS INs. Assuming similar Ca^{2+} sensors and docked vesicle distributions, this would
98 suggest a lower average Ca^{2+} channel density within the AZs of low P_r synapses.

99 Here we tested this hypothesis with two independent methods. 1) Using two-photon Ca^{2+}
100 imaging in hippocampal CA3 PC axon terminals, *post hoc* immunohistochemical
101 identification of their postsynaptic target cells, followed by three-dimensional (3D) EM
102 reconstructions of the imaged boutons we estimated the amount of Ca^{2+} entering the bouton
103 (peak concentration x the bouton volume) and divided it by the AZ area. We refer to this as
104 our ‘functional Ca^{2+} channel density’ estimate. 2) We also measured the densities and
105 distribution of Cav2.1 and Cav2.2 voltage-gated Ca^{2+} channel subunits in presynaptic AZs

106 using SDS-digested freeze-fracture replica immunogold labeling (SDS-FRL) and we refer to it
107 as 'Ca²⁺ channel density'. Finally, we assessed the densities of docked vesicles in boutons
108 with different postsynaptic target cell types using EM tomography.

109

110 **Materials and Methods**

111 *Slice preparation and electrophysiological recordings.* Male Wistar rats (14 – 17 days old, n
112 = 97) were sacrificed by decapitation in accordance with the Hungarian Act of Animal Care
113 and Experimentation (1998, XXVIII, section 243/1998) and with the ethical guidelines of the
114 Institute of Experimental Medicine Protection of Research Subjects Committee. The animals
115 were housed in the vivarium of the Institute of Experimental Medicine in a normal 12 hour /
116 12 hour light / dark cycle. Young experimental animals were kept in a cage with their mother
117 and were used before weaning. Acute hippocampal slices were prepared as published
118 previously (Holderith et al., 2012). Briefly: after decapitation, the brain was quickly removed
119 and placed into an ice-cold cutting solution containing (in mM): sucrose, 205.2; KCl, 2.5;
120 NaHCO₃, 26; CaCl₂, 0.5; MgCl₂, 5; NaH₂PO₄, 1.25; glucose, 10; saturated with 95 % O₂ and
121 5 % CO₂. 300 µm thick horizontal slices were cut from the ventral part of the hippocampus
122 using a Leica Vibratome (Leica VT1200S; Leica Microsystems, Vienna, Austria), incubated
123 in an interface-type holding chamber in ACSF containing in mM: NaCl, 126; KCl, 2.5;
124 NaHCO₃, 26; CaCl₂, 2; MgCl₂, 2; NaH₂PO₄, 1.25; glucose, 10 saturated with 95% O₂ and 5%
125 CO₂ (pH = 7.2 – 7.4) at 36 °C, then kept at 22 – 24 °C. Recordings were carried out in the
126 same ACSF at 22 – 24 °C up to 6 hours after slicing.

127 Cells were visualized using a Femto2D microscope equipped with oblique illumination and a
128 water immersion lens (25X, NA = 1.05, Olympus, Japan or 25X, NA = 1.1, Nikon, Japan).

129 Whole-cell voltage- or current-clamp recordings were performed from CA3 PCs or INs

130 located in the strata oriens and pyramidale using MultiClamp 700A and B amplifiers
131 (Molecular Devices). Recorded traces were filtered at 3 - 4 kHz and digitized on-line at 20
132 kHz. Patch pipettes (resistance 3 – 6 M Ω) were pulled from thick-walled borosilicate glass
133 capillaries with an inner filament. Intracellular solution contained in mM: K-gluconate, 110;
134 KCl, 5; creatine phosphate, 10; HEPES, 10; ATP, 2; GTP, 0.4; biocytin, 5 (pH = 7.3; 290 –
135 300 mOsm). For voltage-clamp recordings of evoked EPSCs in INs, the intracellular solution
136 contained picrotoxin (0.6 - 0.8 mM). For current-clamp recordings and Ca²⁺ imaging in PC
137 axons, 100 or 300 μ M Fluo5F (Molecular Probes) and 20 μ M Alexa594 (Molecular Probes)
138 was added to the intracellular solution.

139 The firing pattern of the INs was determined with a series of 500 ms long hyper- and
140 depolarizing current pulses with amplitudes of 125 - 500 pA. A cell was considered fast
141 spiking if the average firing frequency exceeded 70 Hz. For extracellular stimulation, a
142 unipolar stimulating electrode was placed in the stratum oriens at least 100 μ m away from the
143 soma. Interneurons were held at -70 mV and 5 stimuli (0.2 – 0.3 ms duration, 20 - 200 μ A) at
144 40 or 50 Hz with 30 second inter-stimulus interval (15 – 70 repetitions) were applied. Data
145 from 40 and 50 Hz stimulations were pooled (Fig. 1I). To be able to assess the Elfn1/2
146 expression in mGluR1 α ⁺ cells with different short-term plasticity, cells with inputs exhibiting
147 short-term depression (~10% in the random mGluR1 α ⁺ population) were selectively searched
148 for (Fig. 1J, K). Series resistance was monitored and was < 20 M Ω . Pyramidal cells were held
149 at -70 mV (with a maximum of -100 pA DC current) and single APs at 0.05 – 0.016 Hz were
150 evoked with 2 – 4 ms-long depolarizing current pulses (1 – 1.2 nA). Peak amplitude and full
151 width at half maximal amplitude of the APs were monitored and cells were rejected if any of
152 these parameters changed more than 10%.

153 *Two-photon [Ca²⁺] imaging.* Experiments were performed with a Femto2D (Femtonics Ltd.,
154 Budapest, Hungary) laser scanning microscope equipped with a MaiTai femtosecond pulsing

155 laser tuned to 810 nm (described in Holderith et al., 2012). Electrophysiological data and
156 image acquisition was controlled with a software written in MATLAB (MES, Femtonics Ltd.,
157 Budapest, Hungary). Cells were filled for 2 hours with a Ca^{2+} -insensitive (20 μM Alexa594)
158 and a Ca^{2+} -sensitive fluorophore (100 or 300 μM Fluo5F). Boutons were selected at 150 – 300
159 μm distances from the soma on the second and third order collaterals of the main axon in the
160 stratum oriens at 35 – 80 μm slice depth. They were imaged in line scan mode (scan duration
161 500 or 1200 ms at 1 kHz, 1 - 3 per minute repetition, 2 - 3 scans averaged for each bouton)
162 with a laser intensity of 2 - 6 mW at the back aperture of the objective lens. Single AP-evoked
163 changes in fluorescence were quantified during the recording as $\Delta G/R(t) = (F_{\text{green}(t)} - F_{\text{rest, green}})$
164 $/ (F_{\text{red}} - I_{\text{dark, red}})$ where $F_{\text{green}(t)}$ represents the green fluorescence signal as a function of time,
165 $F_{\text{rest, green}}$ is the green fluorescence before stimulation, and $I_{\text{dark, red}}$ is the dark current in the red
166 channel. To normalize data across batches of dyes, G_{max}/R values were measured by imaging
167 a sealed (tip melted and closed by heating) pipette filled with intracellular solution containing
168 10 mM CaCl_2 for each cell at the same position where the boutons were imaged. $\Delta G/R$
169 measurements from boutons were divided by G_{max}/R , yielding the reported values of G/G_{max} .
170 The effects of 50 μM CdCl_2 and 1 μM ω -CTX MVIIC (diluted in 1 mg/ml BSA; Tocris and
171 Alomone Labs) were tested by comparing the peak amplitudes of presynaptic $[\text{Ca}^{2+}]$ transients
172 in individual boutons averaged from 2-3 consecutive scans in control conditions and after 10
173 (for CdCl_2) or 30 min (for ω -CTX MVIIC) of wash-in of the drug.

174 *Tissue processing.* Following recordings, the slices were fixed in a solution containing 4 %
175 paraformaldehyde (PFA), 0.2% picric acid in 0.1 M phosphate buffer (PB; pH = 7.4) at 4 °C
176 for either 12 - 36 hours (PV or mGluR1 α immunolabeling) or 1-3 hours (for Eln1/2 labeling).
177 Slices containing filled PCs were incubated in 10 and 20% sucrose as cryoprotectant,
178 repeatedly freeze-thawed above liquid nitrogen, embedded in agarose (2%) and re-sectioned

179 at 70 – 90 μm thickness. Slices containing filled INs were immunolabelled without re-
180 sectioning.

181 For quantification of colocalization of mGluR1 α and Elfn1/2 six, and for mGluR1 α and PV
182 three 14 – 17 days old male Wistar rats were deeply anaesthetized and were transcardially
183 perfused with ice cold fixative containing 2 or 4% PFA and 0.2% picric acid in 0.1 M PB for
184 25 minutes. The brains were then quickly removed from the skull and placed in 0.1 M PB. For
185 serial EM reconstructions and EM tomography the fixative contained 2% PFA and 1%
186 glutaraldehyde (GA) in 0.1 M sodium acetate buffer (pH = 6) for 2 minutes, followed by 45
187 minutes of perfusion with 2% PFA and 1% GA in 0.1 M borate buffer (pH = 9) in six 14 – 17
188 days old male Wistar rats. The brains were left in the skull overnight then removed and placed
189 in 0.1 M PB. 60 μm thick sections were cut from the ventral hippocampus.

190 *Light microscopy.* Sections / slices were washed in 0.1M PB and blocked in normal goat
191 serum (NGS, 10%) for 1 hour made up in Tris-buffered saline (TBS; pH 7.4), incubated in the
192 following primary antibodies: mouse anti-PV (1:1000, SWANT; RRID:AB_10000343);
193 rabbit anti-PV (1:1000 Synaptic Systems; RRID:AB_1210396), guinea pig anti-mGluR1 α
194 (1:1000, Frontier Institute Co. Ltd; Mansouri et al., 2015; RRID:AB_2531897) or rabbit anti-
195 Elfn1/2 (1:500, Sigma; RRID:AB_1079280) diluted in TBS containing 2% NGS. After
196 several washes the following secondary antibodies were applied: Alexa488- or Cy5-
197 conjugated goat anti-mouse or goat anti-rabbit, and Cy3-conjugated donkey anti-guinea pig
198 IgGs. Biocytin was visualized with Alexa488- (Molecular Probes) or Cy5- (Jackson
199 Laboratories) conjugated streptavidin (1:500). Sections were mounted in Vectashield. Image
200 stacks were acquired with an Olympus FV1000 confocal microscope with 20x and 60x (oil
201 immersion) objectives. Contacts between PC boutons and IN dendrites were considered as
202 putative synapses if they had no apparent gap between them in the focal plane.

203 *Electron microscopy.* For standard transmission EM and EM tomography, biotinylated goat
204 anti-mouse, goat anti-rabbit and goat anti-guinea pig secondary antibodies were used (Vector
205 Laboratories, 1:50). Reactions and biocytin in the filled cells (after fluorescent examination)
206 were visualized using an avidin-biotin-horseradish peroxidase complex (Vector Laboratories)
207 and 3-3'-diaminobenzidine tetrahydrochloride (DAB) as chromogen. Sections were treated
208 with 1% OsO₄, stained in 1% uranyl acetate, dehydrated in a graded series of ethanol and
209 embedded in epoxy resin (Durcupan). Representative cells were reconstructed using the
210 Neurolucida system (Micro-BrightField Europe, Magdeburg, Germany) attached to a Zeiss
211 Axioscope2 microscope using 40x or 100x oil-immersion objectives. Imaged axon segments
212 were re-embedded and sectioned at 60 nm. Digital images from serial EM sections were taken
213 from the identified imaged boutons or randomly selected PV⁺ or mGluR1 α ⁺ dendrites in the
214 stratum oriens at magnifications of 7500x or 10000x with a Jeol1011 EM. Boutons were 3D
215 reconstructed, and their volumes and the area of the AZ (equal to the corresponding PSD)
216 were measured using the Reconstruct software (<http://synapses.clm.utexas.edu/>). In the case
217 of multiple AZ boutons (12% in PV and 9% in mGluR1 α targeting population), the total AZ
218 area was calculated by summing the individual AZ areas (Fig. 3E).

219 *EM tomography.* 200 nm thick sections were cut and proteinA-conjugated 10 nm gold
220 particles (Cytodiagnostic) were applied on both sides as fiducial markers. Immunolabelled
221 dendritic segments (n = 3 age-matched rats) were randomly selected in the stratum oriens.
222 Single-axis tilt series of perpendicularly oriented synapses were acquired using a Tecnai G2
223 Spirit BioTWIN transmission EM operating at 120 kV and equipped with an Eagle 4K HS
224 digital camera (Fei Europe Nanoport, Eindhoven, The Netherlands). Tilt series were recorded
225 between $\pm 65^\circ$ (with 2° increments between $\pm 45^\circ$ and with 1° increments between ± 45 - 65°)
226 at 30 000x magnification using Fei Xplore3D. Tomographic volumes were reconstructed
227 using the IMOD package (Kremer et al., 1996; Imig et al., 2014), and exported without

228 binning as z-stacks for analysis (320 images per subvolume resulting an 0.6 nm virtual pixel
229 size in Z dimension). AZ area and vesicle distance from the presynaptic membrane were
230 measured with the Reconstruct software. A vesicle was considered to be docked if the outer
231 part of the lipid bilayer was in direct contact with the inner part of the AZ membrane bilayer.
232 A vesicle was considered to be pre-docked if the distance between these lipid bilayers did not
233 exceed 5 nm. The ‘membrane-proximal’ population was pooled from docked and pre-docked
234 populations.

235 *SDS-digested freeze-fracture replica-labeling (SDS-FRL)*. Eight male Wistar rats (P15–17)
236 were deeply anaesthetized and transcardially perfused with a fixative containing 2% PFA and
237 0.2% picric acid in 0.1 M PB for 15 minutes. The brains were then quickly removed from the
238 skull and placed in 0.1 M PB. Horizontal sections of 80 μm thickness were cut from the
239 forebrain with a vibratome and were cryoprotected in 30% glycerol. Small blocks from the
240 ventral CA3 area were frozen with a high-pressure freezing machine (HPM100; Leica
241 Microsystems), fractured with a freeze-fracture machine (BAF060; Leica Microsystems), and
242 processed for SDS-FRL as described previously (Kerti et al., 2012). Tissue debris was
243 digested from the replicas in a TBS solution containing 2.5% SDS and 20% sucrose at 80°C
244 overnight. The replicas were then washed and blocked with 5% BSA in TBS for 1 hour
245 followed by an incubation in a solution of the following primary antibodies: rabbit anti-
246 Cav2.1 (1:500 or 1:600, Synaptic Systems, Cat No. 152 203; RRID:AB_2619841; this Ab
247 provides identical labeling to that of a guinea pig anti-Cav2.1, the specificity of which was
248 proven in Holderith et al., 2012) rabbit anti-Cav2.2 (1:400, Synaptic Systems; Cat No.: 152
249 303; RRID:AB_2619844; specificity of the reaction with this Ab is verified in Lenkey et al.,
250 2015), rabbit anti-Kv3.1b (1:200–1:250, Alomone; RRID:AB_2040166), guinea pig anti-
251 mGluR1 α (1:100, Frontier Institute Co. Ltd; RRID:AB_2531897). Replicas then were washed
252 and incubated in a solution containing the following secondary antibodies: goat anti-rabbit

253 IgGs coupled to 5 or 10 nm gold particles (1:75 or 1:100; British Biocell) and goat anti-guinea
254 pig IgGs coupled to 15 nm gold particles (1:75 or 1:100; British Biocell). Replicas were
255 rinsed in TBS and distilled water before they were picked up on copper parallel bar grids and
256 examined with a Jeol1011 EM. All antibodies used in this study recognized intracellular
257 epitopes on their target proteins and consequently were visualized by gold particles on the P-
258 face. The nonspecific background labeling was measured on surrounding E-face structures.

259 To quantify the Cav2.1 and the Cav2.2 subunit densities in the AZs of axon terminals
260 targeting Kv3.1b⁺ or mGluR1 α ⁺ dendrites, all experiments were performed with the ‘mirror
261 replica method’ (Hagiwara et al., 2005). With this method, replicas are generated from both
262 matching sides of the fractured tissue surface, allowing the examination of the corresponding
263 E- and P-faces of exactly the same membranes. The AZs were delineated on the P-face based
264 on the underlying high density of intramembrane particles. Gold particles inside the synaptic
265 area and up to 30 nm away from its edge were counted. Axon terminals containing Cav
266 subunit labeling without an elevated density of intramembrane particles were discarded from
267 the analysis because this is a characteristic feature of inhibitory terminals (Lenkey et al.,
268 2015). All AZs, fractured partially or in their completeness, were quantified. When the
269 synaptic area was not flat, the replica was tilted. To eliminate reaction-to-reaction variability
270 in the Cav subunit labeling, synaptic, extrasynaptic bouton, and background Cav densities
271 were normalized to the mean of the Cav densities measured in the AZs targeting mGluR1 α ⁺
272 profiles in each reaction.

273 *Analysis of the sub-AZ distribution of immunoreactive Cav2.1 and Cav2.2 subunits.* To
274 investigate whether the within-AZ distribution of gold particles labeling the Cav2.1 or Cav2.2
275 subunits is different from random distributions, we computed two measures with an in-house
276 developed software. First, we calculated the mean of the nearest neighbor distances of all gold
277 particles within an AZ ($\overline{\text{NND}}$) and that of random distributed gold particles within the same

278 AZ (same number of gold particles, 1000 repetitions). The $\overline{\text{NND}}$ s were then statistically
279 compared with Wilcoxon signed-rank test. In our second approach, we computed a two-
280 dimensional spatial autocorrelation function ($g(r)$) for our experimental data and for their
281 random controls based on the methods of Veatch et al. (2012). The $g(r)$ reports the probability
282 of finding a second gold particle at a given r distance away from a given gold (Veatch et al,
283 2012). For randomly distributed gold particles $g(r) = 1$, whereas spatial inhomogeneities result
284 in $g(r)$ values > 1 at short distances. In our experiments, we computed the $g(r)$ for $0 < r < 80$
285 nm, then their mean ($\overline{g(r)}$) was calculated and compared to those obtained from random
286 distributions using the Wilcoxon signed-rank test.

287

288 *Quantification of mGluR1 α and Elfn1/2, and mGluR1 α and PV colocalization.* Colocalization
289 of immunolabelled somata and dendrites was assessed in image stacks acquired with an
290 Olympus FV1000 confocal microscope with 20x (somata) or 60x (dendrites) objectives in
291 randomly selected areas of the CA3 stratum oriens for Elfn1/2, and dorsal and ventral CA1
292 and CA3 areas for PV. Image stacks were acquired at 20X magnification and cells were
293 quantified in ROIs of 200x600x60 μm in the Fluoview software. Image stacks at 60X
294 magnification were imported into the NeuroLucida software, and the total length of single and
295 double labeled dendrites were measured in ROIs of 70x70x36 μm .

296 *Data analysis and statistical tests.* Analysis of electrophysiological and two-photon imaging
297 data was performed using specialized Matlab-based software (MES, Femtonics Ltd. Budapest,
298 Hungary). Data were plotted using OriginPro. Normality of data was assessed using Shapiro-
299 Wilks test; statistical significance was assessed with t -test (independent two-sample with
300 unequal variances, Table 1) when the distribution was not statistically different from normal.
301 For non-normal distributions and when the sample size was small, either Mann Whitney U-
302 test (MW U-test; two unpaired groups, Fig. 2J, 3D, E, Fig. 4O-Q, Fig. 7G, H), or Wilcoxon

303 signed-rank test (two paired groups, Fig. 5 *P, R*, 6 *K, L*), or Kruskal–Wallis test (multiple
304 unpaired groups) with MW U-test with Bonferroni adjustment (2*I* (3 groups), 5*O* (5 groups),
305 6*J* (5 groups)) were used. For the comparison of the short-term plasticity of evoked EPSCs,
306 two-way repeated measures ANOVA with Bonferroni *post hoc* test was used (Fig. 1). Power
307 analysis were performed and predicted a power of 0.8 for every dataset in Fig. 2 and 3 and
308 0.75 for data in Fig. 7. Data are presented as mean \pm standard deviation (SD) for normally
309 distributed data or median and interquartile ranges (IQR) for non-normal distributions. Results
310 were considered significant when $p < 0.05$. In all figures, * $p < 0.05$; ** $p \leq 0.01$; *** $p \leq 0.001$.

311

312 **Results**

313 **Distinct short-term plasticity of EPSCs in different IN types of the hippocampal CA3**

314 **region**

315 We chose CA3 PC local axon collaterals as the subject of our study because they are
316 amenable to presynaptic $[Ca^{2+}]$ measurements (Holderith et al., 2012) and establish synaptic
317 contacts onto both FS, PV positive (PV^+) and mGluR1 α positive (mGluR1 α^+) INs. First we
318 characterized the short-term plasticity of EPSCs recorded from PV^+ and mGluR1 α^+ INs in the
319 CA3 region of young Wistar rats. Whole-cell voltage-clamp recordings were performed from
320 the somata of GABAergic INs located in the stratum oriens with biocytin-containing
321 intracellular solutions and five EPSCs were evoked by extracellular stimulation of PC axons
322 (Fig. 1). The cells were characterized based on their firing patterns (Fig. 1*C, G*), *post hoc*
323 determined dendritic and axonal arbors (Fig. 1*A, E*) and their PV or mGluR1 α
324 immunoreactivity (Fig. 1*B, F*). EPSCs evoked by a train of stimuli at 40 or 50 Hz in PV^+ INs
325 showed short-term depression ($EPSC^{5th} / EPSC^{1st}$: 0.48 ± 0.16 , $n = 10$; Fig. 1*D, I*). In contrast,
326 five stimuli elicited facilitating EPSCs in mGluR1 α^+ INs ($EPSC^{5th} / EPSC^{1st} = 3.0 \pm 1.9$, $n =$

327 31; Fig. 1H, I). Although the mGluR1 α ⁺ cells showed marked heterogeneity based on their
328 dendritic and axonal arbors, firing patterns and short-term plasticity, their excitatory inputs
329 showed a different short-term plasticity pattern when compared to those recorded from PV⁺
330 cells (Fig. 1I). These results clearly demonstrate robust differences in the short-term plasticity
331 of evoked EPSCs in PV⁺ and mGluR1 α ⁺ INs in the CA3 area similar to those observed in the
332 CA1 area and the neocortex, offering the use of these molecules in this brain region as
333 markers to label the postsynaptic compartments of functionally distinct presynaptic axon
334 terminals. Because 75% of mGluR1 α ⁺ cells also contain low amounts of PV in the dorsal
335 hippocampal CA1 area (Ferraguti et al., 2004), we performed colocalization of these two
336 molecules in the dorsal and ventral CA1 and CA3 areas. Our results confirmed those of
337 Ferraguti et al. (2004) revealing $66 \pm 4\%$ and $65 \pm 21\%$ colocalization in the dorsal CA1 and
338 CA3 areas, respectively. However, we found that less than 4% of the mGluR1 α ⁺ cells are
339 immunopositive for PV in the ventral CA3 area. This low prevalence of colocalization was
340 observed in perfusion fixed brain sections ($2.4 \pm 1.7\%$, n = 3 rats) as well as in immersion
341 fixed hippocampal *in vitro* slices ($3.3 \pm 3.5\%$, n = 4 rats).

342 As Efn1 has been demonstrated to play a critical role in the short-term facilitation of EPSCs
343 in mGluR1 α ⁺ O-LM cells of the CA1 region (Sylwestrak and Ghosh, 2012), we performed
344 double immunolocalization for mGluR1 α and Efn1/2 in the stratum oriens of the CA3 area of
345 perfusion fixed rats. We found that almost all ($99 \pm 4\%$) Efn1/2 immunopositive (Efn1/2⁺)
346 dendrites also contained mGluR1 α and that, conversely, $90 \pm 5\%$ of the mGluR1 α ⁺ dendrites
347 were also Efn1/2⁺ (~ 6000 μm dendrite / animal, n = 3 animals). When we tested the short-
348 term plasticity of EPSCs in Efn1/2 and mGluR1 α double labelled INs, they showed a robust
349 short-term facilitation, the degree of which was significantly larger than that detected in
350 mGluR1 α ⁺, but Efn1/2 negative, cells (Fig. 1J, K). These results reveal a previously unseen
351 diversity among mGluR1 α ⁺ INs and provide an explanation for the variance in the short-term

352 plasticity of their inputs. Elfn1/2 seems to be an ideal molecular marker for postsynaptic INs
353 that receive strongly facilitating inputs, but its *post hoc* visualization requires very mild
354 fixation (see Methods) that is incompatible with *post hoc* recovery of axonal arbor and EM
355 analysis. However, because 90% of mGluR1 α ⁺ IN dendrites are also Elfn1/2⁺, we decided to
356 use mGluR1 α as our molecular marker for facilitating synapses.

357 **Target cell type-dependent differences in Ca²⁺ inflow at the AZ**

358 First we opted for a combined functional and morphological approach to estimate the
359 ‘functional Ca²⁺ channel density’ in the presynaptic AZs of CA3 PCs (Holderith et al., 2012).
360 This approach requires the measurements of [Ca²⁺] in local axon terminals of PCs using two-
361 photon microscopy with an intracellularly applied Ca²⁺ sensitive dye (300 μ M Fluo5F; Fig. 2).
362 Single action potential (AP)-evoked [Ca²⁺] transients showed sizeable variability in their peak
363 amplitudes (coefficient of variation (CV) = 0.37, n = 692 boutons in 30 cells). To specifically
364 examine [Ca²⁺] in axon terminals with identified postsynaptic target cell types, we fixed the
365 slices following the *in vitro* imaging experiments and then visualized the intracellular biocytin
366 and immunolabelled the tissue for mGluR1 α and PV for confocal microscopy analysis (Fig.
367 2D-G). In most experiments we imaged 15-30 boutons, out of which few had apparently PV⁺
368 or mGluR1 α ⁺ dendrites as postsynaptic targets. From the total of 692 imaged boutons, we
369 found 26 and 61 as potential presynaptic elements to PV⁺ and mGluR1 α ⁺ INs, respectively.
370 Our *post hoc* analysis revealed that the peak amplitude of the [Ca²⁺] transient was 1.25-times
371 larger in PV⁺ dendrite-targeting boutons compared to their mGluR1 α ⁺ dendrite-targeting
372 counterparts (PV: median: 0.134 G/G_{max}, interquartile ranges (IQR): 0.105 – 0.168 G/G_{max}, n
373 = 26; mGluR1 α : median: 0.107 G/G_{max}, IQR: 0.081 – 0.138 G/G_{max}, n = 61, unidentified
374 target: median: 0.114 G/G_{max}, IQR: 0.084 – 0.145 G/G_{max}, n = 605,; Fig. 2I; Table 1). To
375 minimize potential errors caused by slightly different dye concentrations in distinct PCs, we
376 calculated peak amplitude ratios with two other methods. First, we restricted our analyses to

377 cells that contained both PV⁺ and mGluR1 α ⁺ dendrite-targeting boutons and calculated
378 within-cell ratios, and found a similar 1.28-times higher value in boutons targeting PV⁺
379 dendrites (n = 10 cells). Second, we normalized the peak amplitude of the [Ca²⁺] transients in
380 each PV⁺ and mGluR1 α ⁺ dendrite-innervating bouton to the mean of peak amplitudes
381 recorded from all boutons of a given cell and again found a 1.21-times larger value in boutons
382 targeting PV⁺ dendrites. In a separate set of experiments, we performed [Ca²⁺] imaging with
383 100 μ M Fluo5F and calculated the above mentioned peak amplitude ratios. The within-cell
384 ratio of peak [Ca²⁺] in boutons innervating PV⁺ or mGluR1 α ⁺ dendrites was 1.32 (n = 11 cell),
385 whereas the [Ca²⁺] transients in PV or mGluR1 α -innervating boutons normalized to the mean
386 [Ca²⁺] transients were 1.33 (n = 18) and 1.04 (n = 35), respectively, yielding a ratio of 1.27
387 (Table 1).

388 Because Sylwestrak and Ghosh (2012) reported the presence of kainate receptors in axon
389 terminals innervating mGluR1 α ⁺ O-LM cells that could potentially contribute to the
390 presynaptic [Ca²⁺], we examined the effect of a non-selective voltage-gated Ca²⁺ channel
391 blocker. We found that 50 μ M Cd²⁺ caused a similar reduction in the peak [Ca²⁺] in
392 mGluR1 α ⁺ dendrite-innervating boutons (89 \pm 10 % block n = 8) compared to that of
393 unidentified targets (87 \pm 10% block, n = 36 in n = 4 cells), ruling out a significant cell type-
394 dependent differential contribution of kainate receptors to single AP-evoked presynaptic
395 [Ca²⁺] transients. To assess the contribution of the N/P/Q-type Ca²⁺ channels to the [Ca²⁺]
396 transients we applied ω -CTX MVIIC (a selective N- and P/Q-type Ca²⁺ channel blocker) in a
397 concentration (1 μ M) that almost completely abolishes the evoked EPSCs in both PV⁺ (96 \pm
398 3% block, n = 4 cells) and mGluR1 α ⁺ (93 \pm 7% block, n = 6) INs in the str. oriens of the CA3
399 area. The toxin reduced the peak amplitude of the presynaptic [Ca²⁺] transients by 45 \pm 10%
400 (n = 12 in PV-innervating boutons) and 46 \pm 18% (n = 19 mGluR1 α -innervating boutons),

401 demonstrating a similar contribution of these channels to the $[Ca^{2+}]$ transients in the two
402 bouton populations.

403 A larger $[Ca^{2+}]$ transient might be the consequence of lower Ca^{2+} buffering, a smaller bouton
404 volume, or a larger amount of Ca^{2+} entering the bouton. To assess potential differences in
405 Ca^{2+} buffering in these boutons, which were often only a few microns away from each other
406 (inter-bouton distance: $6.4 \pm 3.5 \mu\text{m}$) on the same axon branch, first we fitted the decay of the
407 grand total averaged $[Ca^{2+}]$ transients with single exponentials and found very similar time
408 constants (PV: 352 ms vs. mGluR1 α : 413 ms). However, the high fluorescent dye
409 concentration (300 μM) used in these experiments might dominate the decay, masking
410 potential differences in the fixed buffer concentration. To circumvent this problem, we
411 recorded $[Ca^{2+}]$ transients with 100 μM Fluo5F and analyzed their decay times (Fig. 2J). The
412 $[Ca^{2+}]$ transients recorded with lower dye concentrations displayed a substantially faster decay
413 (300 μM : 463 ms vs. 100 μM : 210 ms, fitted to the first 260 ms of the averaged traces). When
414 the decay time constants of $[Ca^{2+}]$ transients were compared in boutons innervating PV $^+$ and
415 mGluR1 α^+ dendrites, no significant difference was found (PV: median: 277 ms, IQR: 212 –
416 403 ms, $n = 18$; mGluR1 α : median: 259 ms, IQR: 207 – 322 ms, $n = 35$; $p = 0.61$, MW U-test;
417 Fig. 2J), arguing against a robust difference in Ca^{2+} buffering. To test potential differences in
418 bouton volumes, we carried out 3D EM reconstructions of PV $^+$ or mGluR1 α^+ dendritic
419 segments together with their presynaptic axon terminals in the stratum oriens of perfusion
420 fixed tissue (Fig. 3). Both PV $^+$ and mGluR1 α^+ dendrites were densely innervated by axon
421 terminals, the majority of which formed asymmetrical (excitatory) synapses onto dendritic
422 shafts (Fig. 3A, B). These boutons mainly originate from CA3 PCs located either in the ipsi-
423 or contralateral hemisphere. Three-dimensional reconstructions (Fig. 3C) revealed no
424 significant difference in the volume of the boutons innervating these IN types (PV: median:
425 $0.20 \mu\text{m}^3$, IQR: $0.136 - 0.25 \mu\text{m}^3$, $n = 67$; mGluR1 α : median: $0.20 \mu\text{m}^3$, IQR: $0.125 - 0.291$

426 μm^3 , $n = 87$; $p = 0.65$, MW U-test; Fig. 3D), demonstrating that distinct bouton volumes are
427 not the main cause of the observed differences in peak $[\text{Ca}^{2+}]$. Because previous studies from
428 our laboratory revealed that presynaptic Cav2.1 and Cav2.2 Ca^{2+} channel subunits are
429 confined to the AZ of hippocampal glutamatergic and GABAergic axon terminals (Holderith
430 et al., 2012; Lenkey et al., 2015), we measured the total AZ areas in the 3D reconstructed
431 boutons and found significantly smaller AZs in PV^+ dendrite-innervating boutons (PV:
432 median: $0.06 \mu\text{m}^2$, IQR: $0.04 - 0.08 \mu\text{m}^2$, $n = 67$; mGluR1 α : median: $0.08 \mu\text{m}^2$, IQR: $0.05 -$
433 $0.11 \mu\text{m}^2$, $n = 87$; $p = 0.0001$, MW U-test; Fig. 3E). Finally, we calculated the total Ca^{2+} that
434 enters upon an AP by multiplying the peak $[\text{Ca}^{2+}]$ with the medians of the volume of
435 randomly selected and 3D reconstructed boutons. Assuming that this Ca^{2+} enters through Ca^{2+}
436 channels located in the AZs, we normalized this data to the median AZ area. This way we can
437 calculate the total amount of Ca^{2+} that enters the boutons through a unit AZ area (termed as
438 ‘functional Ca^{2+} channel density’) in PV^+ and mGluR1 α^+ dendrite-targeting boutons and
439 found it to be 1.7-times larger in PV^+ dendrite-innervating boutons.

440 To provide a more direct measure of the ‘functional Ca^{2+} channel density’ in these AZs, we
441 randomly selected a subset of our *in vitro* two-photon imaged boutons with LM
442 immunofluorescent identification of their postsynaptic target cells ($n = 12 \text{PV}^+$ and $n = 18$
443 mGluR1 α^+ -targeting boutons from 9 PCs) and performed serial section EM of the imaged
444 boutons (Fig. 4A-M). This method provides a more accurate ‘functional Ca^{2+} channel density’
445 estimate, but it has the disadvantage of being so labor intensive that a smaller data set was
446 obtained. The peak amplitude of the $[\text{Ca}^{2+}]$ transient in EM-verified PV^+ dendrite-targeting
447 boutons was 1.32-times larger compared to that recorded in mGluR1 α^+ dendrite-targeting
448 boutons (PV: $0.18 \pm 0.06 \text{G}/\text{G}_{\text{max}}$, median: $0.17 \text{G}/\text{G}_{\text{max}}$, $n = 10$; mGluR1 α : 0.13 ± 0.03
449 $\text{G}/\text{G}_{\text{max}}$, median: $0.13 \text{G}/\text{G}_{\text{max}}$, $n = 13$, $p = 0.02$, MW U-test). We could faithfully measure the
450 AZ area in 7 and 10 boutons targeting PV^+ and mGluR1 α^+ dendrites, respectively. In this

451 subset, the peak $[Ca^{2+}]$ in PV^+ dendrite-targeting boutons was 1.34-times larger compared to
452 that in $mGluR1\alpha^+$ dendrite-targeting ones (PV : 0.17 ± 0.05 G/G_{max} , median: 0.17 G/G_{max} , $n =$
453 7 ; $mGluR1\alpha$: 0.13 ± 0.02 G/G_{max} , median: 0.13 G/G_{max} , $n = 10$, $p = 0.045$, MW U-test) similar
454 to the difference observed for the population data (c.f. Fig. 2I, 4N-O). EM analysis of these
455 boutons revealed that they established synapses onto dendritic shafts that received many
456 convergent asymmetrical synapses (implying that they were IN dendrites). None of these
457 boutons had any ultrastructural sign of photodamage; they had only a single AZ and appeared
458 qualitatively similar to those reconstructed from perfusion-fixed tissue. When the AZ area to
459 bouton volume ratio was calculated for this subset of boutons (PV : 0.32 ± 0.08 $1/\mu m$, median:
460 0.31 $1/\mu m$, $n = 7$; $mGluR1\alpha$: 0.47 ± 0.13 $1/\mu m$, median: 0.50 $1/\mu m$, $n = 10$; $p = 0.04$, MW U-
461 test, Fig. 4P), a similar significant difference was observed compared to the larger population
462 obtained from the perfusion-fixed tissue with better ultrastructural preservation (PV : $0.32 \pm$
463 0.13 $1/\mu m$, median: 0.29 $1/\mu m$, $n = 59$; $mGluR1\alpha$: 0.42 ± 0.18 $1/\mu m$, median: 0.40 $1/\mu m$, $n =$
464 79 ; $p < 0.001$, MW U-test, single AZ boutons only). Finally, we calculated the total amount of
465 Ca^{2+} per AZ area for these imaged and EM analyzed boutons and obtained a 1.9-times larger
466 value for the PV^+ dendrite-innervating axon terminals (PV : 0.54 ± 0.12 , median: 0.56 , $n = 7$;
467 $mGluR1\alpha$: 0.28 ± 0.06 , median: 0.27 , $n = 10$; $p = 0.002$, MW U-test; Fig. 4Q). These two
468 combined functional-structural approaches indicated 1.7- and 1.9-times differences in the
469 ‘functional Ca^{2+} channel density’ in the AZs of these two bouton populations. Finally, our EM
470 analysis revealed a similar accuracy in predicting synaptic contacts with confocal microscopy
471 between biocytin filled axon terminals and PV^+ (10 out of 12 boutons) or $mGluR1\alpha^+$ (13 out
472 of 18 boutons) dendrites.

473 **Cav2.1 and Cav2.2 subunit densities in presynaptic AZs as determined with replica**
474 **immunolabeling**

475 In the next set of experiments, we performed SDS-FRL to obtain an independent measure of
476 presynaptic Ca^{2+} channel densities. In order to quantitatively compare the immunogold
477 labeling for Ca^{2+} channel subunits in presynaptic AZs that synapse onto distinct IN types, the
478 postsynaptic targets of the axon terminals need to be identified. This requires the use of the so
479 called face-matched mirror replica technique (Hagiwara et al., 2005) and the molecular
480 identification of the target IN types, because the type of IN from small fractured membrane
481 segments cannot be determined based on morphological features. Following rapid freezing
482 under high pressure, we randomly fractured tissue sections from the CA3 area and created
483 carbon-platinum-carbon replicas of both fractured surfaces (Figs. 5, 6). One replica was
484 immunoreacted to identify IN dendrites and its mirror surface was labeled for a Ca^{2+} channel
485 subunit, and all subcellular structures (dendrites, AZs) were identified in both replicas.
486 Metabotropic GluR1 α is a transmembrane protein that is expressed in the somato-dendritic
487 plasma membrane of hippocampal INs and specific antibodies are available that can be used
488 for replica labeling (Mansouri et al., 2015). PV is a cytoplasmic protein that cannot be
489 detected with SDS-FRL, therefore we identified somato-dendritic regions of PV^+ INs based
490 on the presence of immunogold labeling for the Kv3.1b voltage-gated K^+ channel subunit (Du
491 et al., 1996). Both mGluR1 α and Kv3.1b antibodies recognize intracellular epitopes,
492 therefore, label the protoplasmic-face (P-face) of dendritic plasma membranes (Figs. 5, 6).
493 Many membrane segments are attached to these IN dendrites that represent the extracellular-
494 face (E-face) of presynaptic axon terminals. As our antibodies against Ca^{2+} channel subunits
495 recognize intracellular epitopes (label on the P-face), they cannot be used to localize these
496 channels in these attached axonal E-face membranes. The P-faces of these dendrite-attached
497 presynaptic membranes are present in the 'mirror replicas' (Figs. 5, 6). Because the release of
498 glutamate from these axon terminals are mainly mediated by P/Q- and N-type Ca^{2+} channels
499 (see above), we localized both Cav2.1 and Cav2.2 subunits. The dendrite-attached P-face

500 membrane segments were often labelled for the Cav2.1 subunit and the gold particles were
501 concentrated over areas that had an elevated density of intra-membrane particles,
502 corresponding to the AZs (Fig. 5A-N). The normalized density of gold particles within the
503 AZs was significantly larger than that found in the surrounding E-face plasma membranes
504 (defined as background), while the Cav2.1 subunit density in extrasynaptic bouton membranes
505 was similar to that of the background (Fig. 5O). We performed these experiments in five
506 animals and analyzed a total of 112 and 172 AZs attached to Kv3.1b⁺ and mGluR1 α ⁺
507 dendrites, respectively, in the stratum oriens of the CA3 area. Quantitative comparison of the
508 two AZ populations revealed an overall 1.15-times higher density in Kv3.1b⁺ dendrite-
509 targeting AZs (Fig. 5O; for non-normalized gold densities see Table 1)

510 Next, we conducted the same investigation for the other major Ca²⁺ channel subunit (Cav2.2;
511 Fig. 6). Presynaptic P-face plasma membranes attached to Kv3.1b⁺ (n = 52) or mGluR1 α ⁺ (n =
512 114) dendrites were also heavily labeled for the Cav2.2 subunit (Fig. 6A-I). Gold particles
513 were confined to the AZs, where their densities were significantly higher than the background
514 (Fig. 6J). Cav2.2 subunit densities also showed a 1.20-fold higher values in Kv3.1b⁺
515 compared to mGluR1 α ⁺ dendrite-targeting AZs, but the difference did not reach significance
516 (Fig. 6J; for non-normalized gold densities see Table 1). Finally, we investigated whether the
517 sub-AZ distribution of the gold particles labeling the Cav subunits is compatible with a
518 random process. To test this, we computed two measures (nearest neighbor distance (NND),
519 and a two-dimensional spatial autocorrelation function (ACF), see Methods) and compared
520 the real anti-Cav2.1 immunogold distribution data in 43 Kv3.1b⁺ and 72 mGluR1 α ⁺ dendrite-
521 targeting AZs (fractured in their completeness) to those of random gold distributions. Both
522 NND and ACF analysis revealed that the actual data was significantly different from random
523 distributions (Fig. 5P, R). A similar result was obtained for the Cav2.2 subunit in 21 (Kv3.1b)
524 and 40 (mGluR1 α) AZs (Fig. 6K, L). The significantly lower mean NNDs in both Kv3.1b⁺

525 and mGluR1 α ⁺ dendrite-innervating AZs demonstrate spatial inhomogeneities of gold
526 particles.

527 **Difference in docked vesicle density in PV⁺ and mGluR1 α ⁺ dendrite-innervating boutons**

528 Not only the Ca²⁺ channel density influences the distance between the presynaptic Ca²⁺
529 channels and the Ca²⁺ sensors on the synaptic vesicles, but the density of vesicles docked at
530 the AZ is also a key parameter. The best currently known method to analyze the distribution
531 of synaptic vesicles around the AZ at high resolution is EM tomography (Siksou et al., 2007;
532 Imig et al., 2014). We therefore carried out EM tomography on 200 nm thick resin embedded,
533 perfusion fixed tissue immunoreacted for PV or mGluR1 α (Fig. 7) and estimated the densities
534 of vesicles associated with these two AZ populations. Examining the tomographic sub-
535 volumes at a resolution of 0.6 nm allowed the selection of the Z directional planes where each
536 vesicle is closest to the presynaptic AZ membrane, from which the measurements were
537 performed. We defined a vesicle as docked if it directly contacted the AZ membrane (Fig. 7B,
538 E) or as pre-docked if the vesicle to AZ membrane distance was < 5 nm (Fig. 7C, F).
539 Quantitative comparisons revealed a 1.5- and 1.4-times higher density of docked (Fig. 7G)
540 and membrane-proximal (docked and pre-docked vesicles pooled together; Fig. 7H, Table 1.)
541 vesicles in AZs contacting PV⁺ INs, compared to mGluR1 α ⁺ INs, respectively.

542

543 **Discussion**

544 In the present manuscript, we performed two series of experiments to estimate the densities of
545 Ca²⁺ channels in presynaptic AZs of CA3 PCs contacting two distinct types of IN. First, we
546 carried out a combined functional and morphological investigation to estimate what we call
547 ‘functional Ca²⁺ channel density’ and found an almost 2-fold higher density in the AZs

548 innervating PV⁺ compared to mGluR1 α ⁺ INs. This is the consequence of a larger presynaptic
549 [Ca²⁺] transient, a smaller AZ area and a similar volume of boutons innervating PV⁺ INs. We
550 also determined the densities of immunogold particles labeling the Cav2.1 and Cav2.2 Ca²⁺
551 channel subunits using SDS-FRL and found that PV⁺ dendrite-innervating terminals exhibited
552 only a 1.15-times higher Ca²⁺ channel subunit density. Finally, a 1.5-times higher density of
553 docked vesicles in PV⁺ dendrite-innervating AZs was revealed by EM tomography.

554

555 **Target cell type-dependent differential modulation of Ca²⁺ channel function**

556 Our Ca²⁺ imaging experiments are consistent with the results of Koester and Johnston (2005)
557 who have performed simultaneous paired whole-cell recordings and imaged [Ca²⁺] transients
558 in presynaptic boutons mediating either facilitating or depressing EPSPs in the neocortex.
559 They also observed a larger presynaptic [Ca²⁺] transient in depressing PC to multipolar cell
560 synapses compared to those mediating facilitating EPSPs in bitufted cells. However, the
561 difference in the recorded cortical boutons was more robust than that found in our present
562 study in CA3 PCs. Koester and Johnston (2005) did not provide ultrastructural information
563 regarding the bouton volume or AZ size, so the basis for the difference in [Ca²⁺] between the
564 depressing and facilitating synapses could not be determined. Our data thus extend the current
565 knowledge by demonstrating that the larger [Ca²⁺] in high P_r, FS PV⁺ IN-innervating boutons
566 is not the consequence of a smaller bouton volume, but is caused by a larger amount of Ca²⁺
567 entering the bouton upon an AP. By determining the size of the AZs (where Ca²⁺ channels are
568 concentrated) we can predict the [Ca²⁺] in the vicinity of the release sites. Assuming similar
569 Ca²⁺ channel properties in different P_r boutons, our data predict a 1.7 – 1.9-times higher
570 density of Ca²⁺ channels in high P_r AZs. However, quantitative evaluation of several hundreds
571 of AZs with SDS-FRL for both Cav2.1 (P/Q) and Cav2.2 (N-type) Ca²⁺ channel subunits in

572 AZs that remained physically attached to Kv3.1b⁺ (PV⁺) or mGluR1 α ⁺ somato-dendritic
573 membranes revealed only a ~15% higher Cav subunit density in the Kv3.1b⁺ dendrite-
574 innervating AZs.

575 A potential explanation for the discrepancy between our ‘functional channel density’ and
576 SDS-FRL Cav subunit density estimates is a preferential enrichment of Cav2.3 (R-type)/Cav1
577 (L-type)/Cav3 (T-type) subunits in PV⁺ dendrite-innervating boutons (Parajuli et al., 2012;
578 Carbone et al., 2014). However, our experiments with 1 μ M ω -CTX MVIIC (a concentration
579 that almost fully block the evoked EPSCs in both IN types) revealed an almost identical block
580 of [Ca²⁺] transients in boutons targeting these distinct IN types, arguing against differential
581 contribution of R-, T-, and L-type Ca²⁺ channels to the [Ca²⁺] transients. Another possible
582 explanation for this discrepancy is a differential fixed Ca²⁺ buffer concentration in these two
583 bouton populations. However, the similar decay of the [Ca²⁺] transients (recorded with either
584 300 or 100 μ M Fluo5F) in these bouton populations argues against this possibility. We
585 suggest that differential target cell type-dependent regulation of Ca²⁺ channel function is the
586 most likely mechanism underlying the differences.

587 There are a number of ways to regulate Ca²⁺ channel function. Association with different β
588 subunits promotes different voltage-dependent activation and inactivation (reviewed by
589 Buraei and Yang, 2010). Interactions with SNARE proteins such as syntaxin and SNAP25 at
590 the so called ‘synprint’ motif reduce the channel open probability, whereas additional co-
591 expression of synaptotagmin reverses this effect (Zhong et al., 1999). This suggests a
592 regulatory switch by which presynaptic Ca²⁺ channels bound to Ca²⁺ sensors are functionally
593 enabled, whereas Ca²⁺ channels decoupled from Ca²⁺ sensors are disabled (Eggermann et al.,
594 2012). The AZ protein Munc13, which is involved in vesicle priming processes, has also been
595 found to alter Ca²⁺ inflow by modulating the kinetic properties of Ca²⁺ channels without

596 changing their density (Calloway et al., 2015). Probably the most widely studied modulation
597 of Ca^{2+} channel function is its regulation by presynaptic G-protein-coupled receptors (e.g.
598 mGluRs, A1 adenosine-, α_2 noradrenergic, GABA_B or endocannabinoid receptors; Bean,
599 1989; Dittman and Regehr, 1996; Takahashi et al., 1996; Leao and Von Gersdorff, 2002;
600 Brown et al., 2004; Szabo et al., 2014; Kupferschmidt and Lovinger, 2015). P/Q- and N-type
601 Ca^{2+} channel function is reduced via direct binding of G-protein β/γ -subunits to Ca^{2+} channel
602 β subunits. In a recent study, Anderson et al. (2015) demonstrated that presynaptic β
603 neurexins can transsynaptically reduce tonic endocannabinoid production and increase the P_r
604 of CA1 PC axons by alleviating presynaptic $[\text{Ca}^{2+}]$ from CB1-mediated inhibition. Another
605 way of modulating Ca^{2+} channel function is phosphorylation: CDK5 (kinase) / calcineurin
606 (phosphatase) equilibrium has been shown to set the phosphorylation state of the α_1 subunit of
607 N-type Ca^{2+} channels, which influences the voltage dependence of the open probability of the
608 channel (Su et al., 2012; Kim and Ryan, 2013). Whatever the mechanisms are, they must be
609 able to modulate the function of presynaptic Ca^{2+} channels in a postsynaptic target cell type-
610 dependent manner.

611 The amount of Ca^{2+} entering through presynaptic voltage-gated Ca^{2+} channels is very
612 sensitive to the shape/waveform of the AP (Geiger and Jonas, 2000), and therefore a
613 postsynaptic target cell type-dependent difference in the AP waveform could also explain our
614 results. It remains to be seen whether the AP waveform in boutons (Rowan et al., 2014) that
615 are segregated by only a few microns along the same axon could be sufficiently different to
616 account for the ~30% difference in the $[\text{Ca}^{2+}]$ transient observed in our experiments.

617 The larger amount of Ca^{2+} together with a higher docked vesicle density in high P_r boutons,
618 indicates a higher $[\text{Ca}^{2+}]$ at the Ca^{2+} sensors. Rozov et al. (2001) tested the transmission
619 between cortical PCs and two distinct IN types (multipolar and bitufted) with fast and slow
620 Ca^{2+} buffers. The more robust effect of EGTA (slow buffer) on neurotransmitter release from

621 PC to bitufted compared to multipolar cells predicted a larger physical distance between the
622 Ca^{2+} channels and Ca^{2+} sensors (larger coupling distance) in the low P_r synapse. Our
623 ‘functional Ca^{2+} channel density’ estimate is consistent with this prediction and supports the
624 hypothesis that the mechanisms underlying the low initial P_r and the subsequent short-term
625 facilitation is a large Ca^{2+} channel to Ca^{2+} sensor distance (Neher, 1998; Atwood and
626 Karunanithi, 2002; Eggermann et al., 2012).

627 Another level of complexity might arise from the potential target cell type-dependent
628 differences in the sub-AZ distribution of Ca^{2+} channels (Holderith et al., 2012; Nakamura et
629 al., 2015). Our NND and ACF analysis revealed that Cav2.1 and Cav2.2 subunits show
630 within-AZ distributions that are significantly different from random distributions. Note,
631 however, that the fact that the distribution of gold particles in both AZ populations differ from
632 random does not mean that the sub-AZ distribution of Cav channels is identical in both AZ
633 populations.

634

635 **Target cell type-dependent molecular differences in presynaptic axon terminals**

636 So far, the only known protein with a dramatic difference in its density between low- and
637 high- P_r synapses of a single PC axon is mGluR7 (Shigemoto et al., 1996), making it an ideal
638 candidate through which a low initial P_r and a consequent short-term facilitation could be
639 achieved. The pharmacological blockade of group III mGluRs (including mGluR7) increases
640 the amplitude of evoked EPSCs, but does not change the facilitating phenotype of EPSCs
641 recorded from CA1 mGluR1 α^+ INs (Losonczy et al., 2003), suggesting a tonic, mGluR-
642 mediated reduction of transmitter release from these axon terminals. Similarly, knocking
643 down Elnf1 from somatostatin-positive INs also led to an increase in the amplitude of the 1st
644 EPSC of a train and a reduction in the degree of short-term facilitation, consistent with the

645 results of pharmacological block of mGluR7. Indeed, it has recently been shown that the
646 postsynaptically located Efn1 has a key role in the selective recruitment of mGluR7 to the
647 presynaptic AZs of PC axons that contact somatostatin/mGluR1 α ⁺ INs (Tomioka et al., 2014).
648 However, the short-term plasticity of the mGluR1 α ⁺ dendrite-targeting boutons in mGluR7
649 antagonist or following Efn1 knock-down is still facilitating, very different from that
650 observed in PV⁺ IN-targeting boutons, suggesting that other mechanisms must be involved.
651 These might include the regulation of Ca²⁺ channel function mentioned above or the selective
652 presence of molecules that might impose facilitation on synapses (e.g. NMDA receptors,
653 Buchanan et al., 2012; kainate receptors, Sylwestrak and Ghosh, 2012; synaptotagmin-7,
654 Jackman et al., 2016). Additional factors could contribute to differences in initial P_r by
655 changing the sensitivity of the release machinery to [Ca²⁺]. Proteins like Rab3A-D and
656 Munc13-3 increase (Schluter et al., 2004; Schluter et al., 2006; Ishiyama et al., 2014) whereas
657 others such as mover decrease (Korber et al., 2015) P_r without affecting the readily releasable
658 pool. Unc13 isoforms have been implicated in the preferential targeting of vesicles to docking
659 sites that are formed at varying distances from the Ca²⁺ channels (Bohme et al., 2016). Any of
660 these mechanisms may also contribute to the differences in initial P_r in addition to the above
661 described differences in [Ca²⁺].

662 **References**

- 663 Ali AB, Thomson AM (1998) Facilitating pyramid to horizontal oriens-alveus interneurone
664 inputs: dual intracellular recordings in slices of rat hippocampus. *J Physiol (London)*
665 507:185-199.
- 666 Ali AB, Deuchars J, Pawelzik H, Thomson AM (1998) CA1 pyramidal to basket and
667 bistratified cell EPSPs: dual intracellular recordings in rat hippocampal slices. *J*
668 *Physiol (London)* 507:201-217.
- 669 Anderson GR, Aoto J, Tabuchi K, Foldy C, Covy J, Yee AX, Wu D, Lee SJ, Chen L,
670 Malenka RC, Sudhof TC (2015) beta-Neurexins Control Neural Circuits by
671 Regulating Synaptic Endocannabinoid Signaling. *Cell* 162:593-606.
- 672 Atwood HL, Karunanithi S (2002) Diversification of synaptic strength: presynaptic elements.
673 *Nature Rev Neurosci* 3:497-516.
- 674 Bean BP (1989) Neurotransmitter inhibition of neuronal calcium currents by changes in
675 channel voltage dependence. *Nature* 340:153-156.
- 676 Biro AA, Holderith NB, Nusser Z (2005) Quantal size is independent of the release
677 probability at hippocampal excitatory synapses. *J Neurosci* 25:223-232.
- 678 Bohme MA, Beis C, Reddy-Alla S, Reynolds E, Mampell MM, Grasskamp AT, Lutzkendorf
679 J, Bergeron DD, Driller JH, Babikir H, Gottfert F, Robinson IM, O'Kane CJ, Hell SW,
680 Wahl MC, Stelzl U, Loll B, Walter AM, Sigrist SJ (2016) Active zone scaffolds
681 differentially accumulate Unc13 isoforms to tune Ca²⁺ channel-vesicle coupling. *Nat*
682 *Neurosci* 19:1311-1320.
- 683 Brown SP, Safo PK, Regehr WG (2004) Endocannabinoids inhibit transmission at granule
684 cell to Purkinje cell synapses by modulating three types of presynaptic calcium
685 channels. *J Neurosci* 24:5623-5631.
- 686 Buchanan KA, Blackman AV, Moreau AW, Elgar D, Costa RP, Lalanne T, Tudor Jones AA,
687 Oyrer J, Sjostrom PJ (2012) Target-specific expression of presynaptic NMDA
688 receptors in neocortical microcircuits. *Neuron* 75:451-466.
- 689 Buraei Z, Yang J (2010) The β subunit of voltage-gated Ca²⁺ channels. *Physiological Reviews*
690 90:1461-1506.
- 691 Calloway N, Gouzer G, Xue M, Ryan TA (2015) The active-zone protein Munc13 controls
692 the use-dependence of presynaptic voltage-gated calcium channels. *eLife* 4.
- 693 Carbone E, Calorio C, Vandael DH (2014) T-type channel-mediated neurotransmitter release.
694 *Pflugers Arch* 466:677-687.

- 695 Dittman JS, Regehr WG (1996) Contributions of calcium-dependent and calcium-independent
696 mechanisms to presynaptic inhibition at a cerebellar synapse. *J Neurosci* 16:1623-
697 1633.
- 698 Du J, Zhang L, Weiser M, Rudy B, McBain CJ (1996) Developmental expression and
699 functional characterization of the potassium-channel subunit Kv3.1b in parvalbumin-
700 containing interneurons in the rat hippocampus. *J Neurosci* 16:506-518.
- 701 Eggermann E, Bucurenciu I, Goswami SP, Jonas P (2012) Nanodomain coupling between
702 Ca(2+) channels and sensors of exocytosis at fast mammalian synapses. *Nature Rev*
703 *Neurosci* 13:7-21.
- 704 Ferraguti F, Cobden P, Pollard M, Cope D, Shigemoto R, Watanabe M, Somogyi P (2004)
705 Immunolocalization of metabotropic glutamate receptor 1 α (mGluR1 α) in distinct
706 classes of interneuron in the CA1 region of the rat hippocampus. *Hippocampus*
707 14:193-215.
- 708 Geiger JR, Jonas P (2000) Dynamic control of presynaptic Ca²⁺ inflow by fast-inactivating K⁺
709 channels in hippocampal mossy fiber boutons. *Neuron* 28:927-939.
- 710 Hagiwara A, Fukazawa Y, Deguchi-Tawarada M, Ohtsuka T, Shigemoto R (2005)
711 Differential distribution of release-related proteins in the hippocampal CA3 area as
712 revealed by freeze-fracture replica labeling. *J Comp Neurol* 489:195-216.
- 713 Holderith N, Lorincz A, Katona G, Rozsa B, Kulik A, Watanabe M, Nusser Z (2012) Release
714 probability of hippocampal glutamatergic terminals scales with the size of the active
715 zone. *Nature Neurosci* 15:988-997.
- 716 Imig C, Min SW, Krinner S, Arancillo M, Rosenmund C, Sudhof TC, Rhee J, Brose N,
717 Cooper BH (2014) The morphological and molecular nature of synaptic vesicle
718 priming at presynaptic active zones. *Neuron* 84:416-431.
- 719 Ishiyama S, Schmidt H, Cooper BH, Brose N, Eilers J (2014) Munc13-3 superprimed synaptic
720 vesicles at granule cell-to-basket cell synapses in the mouse cerebellum. *J Neurosci*
721 34:14687-14696.
- 722 Jackman SL, Turecek J, Belinsky JE, Regehr WG (2016) The calcium sensor synaptotagmin 7
723 is required for synaptic facilitation. *Nature* 529:88-91.
- 724 Kerti K, Lorincz A, Nusser Z (2012) Unique somato-dendritic distribution pattern of Kv4.2
725 channels on hippocampal CA1 pyramidal cells. *Eur J Neurosci* 35:66-75.
- 726 Kim SH, Ryan TA (2013) Balance of calcineurin A α and CDK5 activities sets release
727 probability at nerve terminals. *J Neurosci* 33:8937-8950.

- 728 Koester HJ, Johnston D (2005) Target cell-dependent normalization of transmitter release at
729 neocortical synapses. *Science* 308:863-866.
- 730 Korber C, Horstmann H, Venkataramani V, Herrmannsdorfer F, Kremer T, Kaiser M,
731 Schwenger DB, Ahmed S, Dean C, Dresbach T, Kuner T (2015) Modulation of
732 Presynaptic Release Probability by the Vertebrate-Specific Protein Mover. *Neuron*
733 87:521-533.
- 734 Kremer JR, Mastrorarde DN, McIntosh JR (1996) Computer visualization of three-
735 dimensional image data using IMOD. *J Struct Biol* 116:71-76.
- 736 Kupferschmidt DA, Lovinger DM (2015) Inhibition of presynaptic calcium transients in
737 cortical inputs to the dorsolateral striatum by metabotropic GABA_B and mGlu2/3
738 receptors. *J Physiol (London)* 593:2295-2310.
- 739 Leao RM, Von Gersdorff H (2002) Noradrenaline increases high-frequency firing at the calyx
740 of Held synapse during development by inhibiting glutamate release. *J Neurophysiol*
741 87:2297-2306.
- 742 Lenkey N, Kirizis T, Holderith N, Mate Z, Szabo G, Vizi ES, Hajos N, Nusser Z (2015) Tonic
743 endocannabinoid-mediated modulation of GABA release is independent of the CB1
744 content of axon terminals. *Nat Comm* 6:6557.
- 745 Losonczy A, Somogyi P, Nusser Z (2003) Reduction of excitatory postsynaptic responses by
746 persistently active metabotropic glutamate receptors in the hippocampus. *J*
747 *Neurophysiol* 89:1910-1919.
- 748 Losonczy A, Zhang L, Shigemoto R, Somogyi P, Nusser Z (2002) Cell type dependence and
749 variability in the short-term plasticity of EPSCs in identified mouse hippocampal
750 interneurons. *J Physiol (London)* 542:193-210.
- 751 Mansouri M, Kasugai Y, Fukazawa Y, Bertaso F, Raynaud F, Perroy J, Fagni L, Kaufmann
752 WA, Watanabe M, Shigemoto R, Ferraguti F (2015) Distinct subsynaptic localization
753 of type 1 metabotropic glutamate receptors at glutamatergic and GABAergic synapses
754 in the rodent cerebellar cortex. *Eur J Neurosci* 41:157-167.
- 755 Markram H, Wang Y, Tsodyks M (1998a) Differential signaling via the same axon of
756 neocortical pyramidal neurons. *Proc Natl Acad Sci USA* 95:5323-5328.
- 757 Markram H, Gupta A, Uziel A, Wang Y, Tsodyks M (1998b) Information processing with
758 frequency-dependent synaptic connections. *Neurobiol Learn Mem* 70:101-112.
- 759 Mercer A, Eastlake K, Trigg HL, Thomson AM (2012) Local circuitry involving
760 parvalbumin-positive basket cells in the CA2 region of the hippocampus.
761 *Hippocampus* 22:43-56.

- 762 Nakamura Y, Harada H, Kamasawa N, Matsui K, Rothman JS, Shigemoto R, Silver RA,
763 DiGregorio DA, Takahashi T (2015) Nanoscale distribution of presynaptic Ca^{2+}
764 channels and its impact on vesicular release during development. *Neuron* 85:145-158.
- 765 Neher E (1998) Vesicle pools and Ca^{2+} microdomains: new tools for understanding their roles
766 in neurotransmitter release. *Neuron* 20:389-399.
- 767 Parajuli LK, Nakajima C, Kulik A, Matsui K, Schneider T, Shigemoto R, Fukazawa Y (2012)
768 Quantitative regional and ultrastructural localization of the Cav2.3 subunit of R-type
769 calcium channel in mouse brain. *J Neurosci* 32:13555-13567.
- 770 Pouille F, Scanziani M (2004) Routing of spike series by dynamic circuits in the
771 hippocampus. *Nature* 429:717-723.
- 772 Reyes A, Lujan R, Rozov A, Burnashev N, Somogyi P, Sakmann B (1998) Target-cell-
773 specific facilitation and depression in neocortical circuits. *Nature Neurosci* 1:279-285.
- 774 Rowan MJ, Tranquil E, Christie JM (2014) Distinct Kv channel subtypes contribute to
775 differences in spike signaling properties in the axon initial segment and presynaptic
776 boutons of cerebellar interneurons. *J Neurosci* 34:6611-6623.
- 777 Rozov A, Burnashev N, Sakmann B, Neher E (2001) Transmitter release modulation by
778 intracellular Ca^{2+} buffers in facilitating and depressing nerve terminals of pyramidal
779 cells in layer 2/3 of the rat neocortex indicates a target cell-specific difference in
780 presynaptic calcium dynamics. *J Physiol (London)* 531:807-826.
- 781 Scanziani M, Gahwiler BH, Charpak S (1998) Target cell-specific modulation of transmitter
782 release at terminals from a single axon. *Proc Natl Acad Sci USA* 95:12004-12009.
- 783 Schluter OM, Basu J, Sudhof TC, Rosenmund C (2006) Rab3 superprimes synaptic vesicles
784 for release: implications for short-term synaptic plasticity. *J Neurosci* 26:1239-1246.
- 785 Schluter OM, Schmitz F, Jahn R, Rosenmund C, Sudhof TC (2004) A complete genetic
786 analysis of neuronal Rab3 function. *J Neurosci* 24:6629-6637.
- 787 Shigemoto R, Kulik A, Roberts JD, Ohishi H, Nusser Z, Kaneko T, Somogyi P (1996) Target-
788 cell-specific concentration of a metabotropic glutamate receptor in the presynaptic
789 active zone. *Nature* 381:523-525.
- 790 Siksou L, Rostaing P, Lechaire JP, Boudier T, Ohtsuka T, Fejtova A, Kao HT, Greengard P,
791 Gundelfinger ED, Triller A, Marty S (2007) Three-dimensional architecture of
792 presynaptic terminal cytomatrix. *J Neurosci* 27:6868-6877.
- 793 Su SC, Seo J, Pan JQ, Samuels BA, Rudenko A, Ericsson M, Neve RL, Yue DT, Tsai LH
794 (2012) Regulation of N-type voltage-gated calcium channels and presynaptic function
795 by cyclin-dependent kinase 5. *Neuron* 75:675-687.

- 796 Sylwestrak EL, Ghosh A (2012) Elfn1 regulates target-specific release probability at CA1-
797 interneuron synapses. *Science* 338:536-540.
- 798 Szabo GG, Lenkey N, Holderith N, Andrasi T, Nusser Z, Hajos N (2014) Presynaptic calcium
799 channel inhibition underlies CB1 cannabinoid receptor-mediated suppression of
800 GABA release. *J Neurosci* 34:7958-7963.
- 801 Takahashi T, Forsythe ID, Tsujimoto T, Barnes-Davies M, Onodera K (1996) Presynaptic
802 calcium current modulation by a metabotropic glutamate receptor. *Science* 274:594-
803 597.
- 804 Thomson AM (1997) Activity-dependent properties of synaptic transmission at two classes of
805 connections made by rat neocortical pyramidal axons in vitro. *J Physiol (London)*
806 502:131-147.
- 807 Tomioka NH, Yasuda H, Miyamoto H, Hatayama M, Morimura N, Matsumoto Y, Suzuki T,
808 Odagawa M, Odaka YS, Iwayama Y, Won Um J, Ko J, Inoue Y, Kaneko S, Hirose S,
809 Yamada K, Yoshikawa T, Yamakawa K, Aruga J (2014) Elfn1 recruits presynaptic
810 mGluR7 in trans and its loss results in seizures. *Nat Comm* 5:4501.
- 811 Veatch SL, Machta BB, Shelby SA, Chiang EN, Holowka DA, Baird BA (2012) Correlation
812 functions quantify super-resolution images and estimate apparent clustering due to
813 over-counting. *PLoS One* 7:e31457.
- 814 Zhong H, Yokoyama CT, Scheuer T, Catterall WA (1999) Reciprocal regulation of P/Q-type
815 Ca^{2+} channels by SNAP-25, syntaxin and synaptotagmin. *Nature Neurosci* 2:939-941.
816

817 **Table1:** Properties of $[Ca^{2+}]$ transients, bouton volumes, AZ areas and Cav
 818 immunoreactivities in PV⁺ and mGluR1 α ⁺ dendrite-innervating axon terminals.

	PV ⁺ dendrite-targeting boutons					mGluR1 α ⁺ dendrite-targeting boutons					Test	p
	Mean	SD	Median	n	# animal	Mean	SD	Median	n	# animal		
Peak amplitude of $[Ca^{2+}]$ transient (300 μ M Fluo5F) (G/G _{max})	0.14	0.05	0.13	26*	15	0.11	0.04	0.11	61*	23	MW U-test	0.012
Normalized peak amplitude of $[Ca^{2+}]$ transient (300 μ M Fluo5F) ¹	1.20	0.41	1.12	26*	15	1.00	0.28	0.98	61*	23	t-test	0.024
Peak amplitude of $[Ca^{2+}]$ transient (100 μ M Fluo5F) (G/G _{max})	0.21	0.10	0.22	14*	9	0.17	0.11	0.14	21*	13	MW U-test	0.100
Normalized peak amplitude of $[Ca^{2+}]$ transient (100 μ M Fluo5F) ¹	1.33	0.51	1.36	18*	12	1.04	0.25	1.03	35*	18	t-test	0.037
Bouton volume in perfused tissue (μ m ³)	0.20	0.10	0.20	67*	3	0.25	0.18	0.20	87*	3	MW U-test	0.650
Bouton volume <i>in vitro</i> slices (μ m ³)	0.31	0.12	0.26	7	5	0.20	0.12	0.18	10	4		
Total AZ area in perfused tissue (μ m ²)	0.06	0.03	0.06	67*	3	0.09	0.05	0.08	87*	3	MW U-test	0.000
AZ area <i>in vitro</i> slices (μ m ²)	0.10	0.04	0.09	7	5	0.09	0.03	0.09	10	4		
Cav2.1 subunit density in AZs (gold/ μ m ²) ²	373	47	370	112	5	321	46	325	172	5		
Cav2.2 subunit density in AZs (gold/ μ m ²) ²	151	30	139	52	4	130	39	130	114	4		
Cav2.1 subunit density in extrasynaptic membranes (gold/ μ m ²) ²	2.14	2.46	2.21	93	5	2.88	2.64	2.23	174	5		
Cav2.2 subunit density in extrasynaptic membranes (gold/ μ m ²) ²	2.69	3.15	2.35	48	4	1.02	1.26	0.75	113	4		
Background Cav2.1 subunit density (gold/ μ m ²) ²	2.27	1.93	2.94	132	5	2.27	1.93	2.94	132	5		
Background Cav2.2 subunit density (gold/ μ m ²) ²	0.66	0.33	0.62	104	4	0.66	0.33	0.62	104	4		
Cav2.1 NND distance (nm)	24.7	4.0	23.3	43	5	24.3	4.6	23.1	72	5		
Cav2.2 NND distance (nm)	32.1	7.2	30.3	21	4	32.0	8.3	28.7	40	4		
Docked vesicle density (vesicle/ μ m ²)	33.1	21.1	35.5	47*	3	21.9	17.5	22.2	49*	3	MW U-test	0.010
Membrane proximal vesicle density (vesicle/ μ m ²)	64.9	42.0	59.1	47*	3	47.3	26.6	49.9	49*	3	MW U-test	0.037

819
 820
 821
 822
 823

* indicates the 'n' used for the statistical comparisons. ¹: $[Ca^{2+}]$ transients were normalized to the mean of all measured $[Ca^{2+}]$ transients of the given cell. ²: Values calculated from the medians of 5 (Cav2.1) and 4 (Cav2.2) rats.

824 **Figure Legends**

825 **Figure 1.** Short-term plasticity of CA3 pyramidal cell synapses contacting PV⁺ or mGluR1 α ⁺
826 interneurons. **A**, NeuroLucida reconstruction of an *in vitro* recorded basket cell in stratum
827 pyramidale (str. pyr.) of the CA3 region of the hippocampus (soma and dendrites orange, axon
828 black). **B**, Confocal image of the biocytin filled interneuron (IN, left) showing
829 immunoreactivity for PV (right). Arrows indicate PV immunoreactivity of the biocytin filled
830 boutons. **C**, Membrane potential responses upon de- and hyperpolarizing current injections.
831 The depolarizing suprathreshold response shows fast spiking (FS) characteristics. **D**,
832 Excitatory postsynaptic currents (EPSC, average of 20 traces) evoked by extracellular
833 stimulation in the stratum oriens (str. ori.) display short-term depression. **E**, NeuroLucida
834 reconstruction of an *in vitro* recorded and biocytin filled oriens-bistratified IN (soma and
835 dendrites blue, axon black) in the str. ori. **F**, The biocytin filled cell (left) is intensely labeled
836 for mGluR1 α (right). **G**, Membrane potential responses to hyper- and depolarizing current
837 pulses. Firing pattern shows moderate spike frequency adaptation and amplitude
838 accommodation. Note the prominent sag and the slow membrane time constant in response to
839 the hyperpolarizing current step. **H**, Extracellular stimulation-evoked EPSCs display short-
840 term facilitation (average of 20 traces). **I**, The short-term plasticity of evoked EPSCs onto PV
841 and mGluR1 α positive INs differs significantly ($p < 0.01$ for cell type, $p = 0.2$ for stimulus
842 number and $p = 0.01$ for cell type and stimulus number interaction, two-way repeated
843 measures ANOVA, Bonferroni *post hoc* test). **J** A biocytin filled IN is intensely labeled for
844 mGluR1 α and Eln1/2. **K**, Peak amplitudes of evoked EPSCs onto mGluR1 α and Eln1/2
845 double positive INs are significantly larger ($p < 0.05$ for cell type, $p = 0.31$ for stimulus
846 number and $p = 0.17$ for cell type and stimulus number interaction, two-way repeated
847 measures ANOVA, Bonferroni *post hoc* test) than those recorded from mGluR1 α positive, but

848 Elfn1/2 negative cells. str. luc., stratum lucidum; str. rad., stratum radiatum; str. l-m, stratum
849 lacunosum-moleculare. Data are presented as mean \pm SD.

850

851 **Figure 2.** Larger $[Ca^{2+}]$ transients in PV^+ than in $mGluR1\alpha^+$ dendrite-contacting boutons. **A**,
852 Two-photon (2P) image stack of a CA3 PC basal dendritic tree and axonal arbor filled with 20
853 μ M Alexa Fluor 594 (Alexa594, red), 300 μ M Fluo5F and biocytin. Boxed area is shown at
854 higher magnification in panel **C**. Cartoon at the upper left corner illustrates the position of the
855 cell in the CA3 area. **B**, Neurolucida reconstruction of the cell shown in panel **A**. Boxed areas
856 correspond to panels **A** and **C**. **C-D**, High magnification two-photon (**C**) and confocal (**D**)
857 images of the scanned axon collaterals following fixation and visualization of the biocytin.
858 Numbers indicate the boutons that have been line scanned. Inset in **C** shows bouton #1 at a
859 higher magnification. The line indicates the position of the line scan. **E-G**, Some of the
860 imaged boutons are in contact with PV (**E-F**, boutons #6 and #12) or $mGluR1\alpha$ (**G**, boutons
861 #15 and #16) immunolabeled dendrites (biocytin: white, PV: orange, $mGluR1\alpha$: cyan). **H**,
862 Single action potential-evoked $[Ca^{2+}]$ transients (n = 16 transients from 16 boutons, each trace
863 is the average of 2 scans) recorded in the axon terminals shown in panel **C**. Orange and cyan
864 traces are transients from PV^+ and $mGluR1\alpha^+$ dendrite-contacting boutons, respectively. Inset
865 shows the same traces after Gauss filtering on an extended time scale. **I**, The peak $[Ca^{2+}]$
866 transient amplitudes are significantly larger (Kruskal-Wallis test: $p = 0.01$, MW U *post hoc*
867 test, $p = 0.01$ between unidentified and PV and $p = 0.01$ between PV and $mGluR1\alpha$) in PV^+
868 (orange) than in $mGluR1\alpha^+$ dendrite-contacting (cyan) or all other boutons (grey, n = 605
869 boutons from 30 cells). Black symbols correspond to individual data points obtained from the
870 cell shown in panels **A-G**. **J**, Averaged $[Ca^{2+}]$ transients, recorded with 100 μ M Fluo5F, in
871 PV^+ (orange) or $mGluR1\alpha^+$ (cyan) dendrite-targeting boutons. Mono-exponential fits show
872 similar decay kinetics. Inset shows the individual decay time constant values in 18 PV^+ and 35

873 mGluR1 α ⁺ dendrite-innervating boutons. The two populations are not significantly different
874 ($p = 0.61$, MW U-test). Circles indicate individual boutons, the boxes represent interquartile
875 ranges with the horizontal bars showing the medians.

876

877 **Figure 3.** Three dimensional reconstructions of PC axon terminals targeting PV⁺ or
878 mGluR1 α ⁺ dendrites. **A, B**, Electron micrograph of a PV⁺ (orange, **A**) and an mGluR1 α ⁺
879 (cyan, **B**) dendrite (labeled with pre-embedding peroxidase reaction, dark precipitate)
880 receiving several excitatory inputs from presynaptic boutons (b). Arrowheads demarcate the
881 postsynaptic densities. **C**, Representative dendritic segments are reconstructed in 3D. Boutons
882 are white and postsynaptic dendrites are orange (PV⁺) or cyan (mGluR1 α ⁺). **D, E**, Bouton
883 volume is not ($p = 0.65$ MW U-test, **D**), but the total active zone area is significantly ($p =$
884 0.0001 MW U-test, **E**) different between PV⁺ and mGluR1 α ⁺ dendrite-targeting terminals.
885 Circles indicate individual boutons, the boxes represent interquartile ranges with the
886 horizontal bars showing the medians.

887

888 **Fig. 4.** Combined functional and morphological analyses of individual boutons show
889 differences in the amount of Ca²⁺ in PC axon terminals innervating PV⁺ or mGluR1 α ⁺ INs. **A**,
890 NeuroLucida reconstruction of a CA3 PC filled with 20 μ M Alexa 594, 300 μ M Fluo5F and
891 biocytin. **B**, Low magnification 2P microscopic image stack of the basal dendritic tree and the
892 axonal arbor of the cell. **C**, Low magnification confocal image stack of the same cell. Boxed
893 areas on panels **A-C** indicate the axon collaterals where 21 boutons were imaged. **D-I**, High
894 magnification views of the two imaged axon collaterals (2P images: **D** and **G**, corresponding
895 confocal images: **E** and **H**, corresponding transmission LM images: **F** and **I**). Inset in panel **E**
896 shows the same axonal arbor at a lower magnification. Arrows indicate those boutons that
897 contacted either mGluR1 α (#1-2 and #4) or PV (#3) immunopositive dendrites. **J**,

898 Immunofluorescent labeling for mGluR1 α (cyan), PV (orange) and biocytin (white) of the
899 imaged area. Arrows point to boutons that form putative synapses on the labeled dendrites. **K**,
900 Correlated electron micrographs of the boutons shown in panel **J**. Arrowheads demarcate the
901 edges of the morphologically identified postsynaptic densities. **L**, Three-dimensional
902 reconstructions of the boutons shown in panels **J** and **K**. Light blue indicates the active zone,
903 dark grey deciphers mitochondria. **M**, Individual [Ca²⁺] transients (average of 2 scans)
904 recorded in the same boutons. **N**, **O**, Calcium transients in boutons with EM reconstructed
905 AZs (**N**: individual transients: semitransparent, mean: bold; PV: orange, n = 7, mGluR1 α :
906 cyan, n = 10). The peak amplitude of the [Ca²⁺] transients is 1.3 times larger in PV (orange),
907 compared to mGluR1 α (cyan) targeting boutons (p = 0.045 MW U-test, black circles
908 correspond to data points obtained from the cell shown in panels **A-M**). Grey symbols indicate
909 average [Ca²⁺] transients of the two bouton populations that were verified with confocal
910 microscopy only (values are from **Figure 2I**). **P**, The active zone area normalized to the
911 bouton volume was significantly (p = 0.04 MW U-test) larger in mGluR1 α ⁺ (n = 10) than in
912 PV⁺ (n = 7) dendrite-targeting boutons similar to the population averages (grey symbols, p <
913 0.0001 MW U-test). **Q**, Calculated total Ca²⁺ per AZ area is twice as large in PV⁺ (n = 7) as in
914 mGluR1 α ⁺ (n = 10) dendrite-targeting boutons (p = 0.002, MW U-test). Data are presented as
915 mean \pm SD.

916

917 **Figure 5.** The density of Cav2.1 subunits is 1.15-times larger in the AZs of Kv3.1b⁺
918 compared to mGluR1 α ⁺ dendrite-targeting boutons. **A**, **B**, Corresponding EM protoplasmic-
919 (PF) and exoplasmic-face (EF) images of a Kv3.1b⁺ (expressed in PV⁺ cells) cell receiving
920 several excitatory inputs (orange on panel **B**). **C**, **D**, Higher magnification images of the boxed
921 areas in **A** and **B** show a perisomatic EF membrane with attached PF fragments of axon
922 terminals (b_{PF}) containing AZs (orange in **D**). Active zones are indicated by the loose cluster

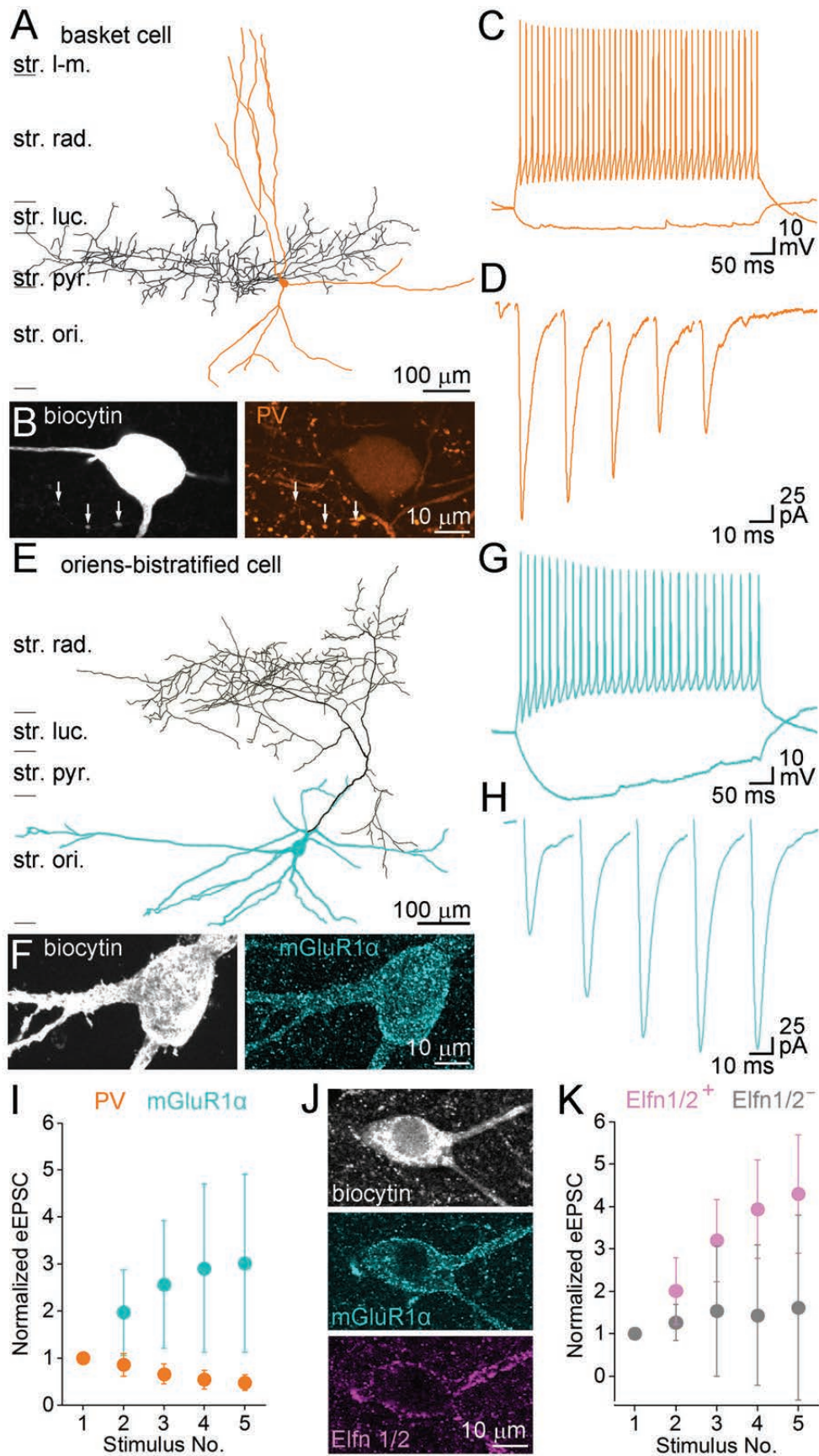
923 of intramembrane particles. **E**, Higher magnification view of the boxed areas in **D**. **F-H**,
 924 Another example of an intensely Cav2.1 labelled AZ attached to a Kv3.1b⁺ dendrite. **I, J**, PF
 925 and EF images of an mGluR1 α immunoreactive dendrite contacted by axon terminals with
 926 AZs (cyan in **J**). **K**, A higher magnification image of the boxed area in **J**. **L-N**, Another
 927 mGluR1 α ⁺ dendrite-attached AZ with intense Cav2.1 labeling. **O**, Normalized densities of
 928 gold particles labeling the Cav2.1 subunit within presynaptic AZ (syn.), extrasynaptic bouton
 929 membranes (extrasyn.) and surrounding EF membranes (background: bg., grey) obtained from
 930 5 rats. *Post hoc* MW U-tests with Bonferroni correction after Kruskal-Wallis test ($p <$
 931 0.0001) demonstrated a significant difference between the synaptic and background labeling
 932 ($p < 0.0001$) and between the synaptic compartments of Kv3.1b⁺ and mGluR1 α ⁺ dendrite
 933 targeting boutons ($p < 0.001$). Circles indicate individual measurements of AZs, the boxes
 934 represent interquartile ranges with the horizontal bars showing the medians. **P**, The nearest
 935 neighbor distance (NND) was calculated for each gold particle within an AZ and the mean
 936 value (\overline{NND}) is plotted against the \overline{NND} of randomly placed gold particles (repeated 1000
 937 times) for each AZ contacting Kv3.1b⁺ ($n = 43$) or mGluR1 α ⁺ ($n = 72$) dendrites. Wilcoxon
 938 signed-rank test revealed significant difference ($p < 0.0001$) between the data and the random
 939 distributions for both AZ populations. **R**, Comparison of the mean two dimensional spatial
 940 autocorrelation functions ($\overline{g(r)}$) measured in individual Kv3.1b⁺ ($n = 43$) or mGluR1 α ⁺ ($n =$
 941 72) dendrite-targeting AZs to their simulated random controls (repeated 1000 times).
 942 Wilcoxon signed-rank test revealed significant differences ($p < 0.0001$) between the data and
 943 the random distributions for both AZ populations.

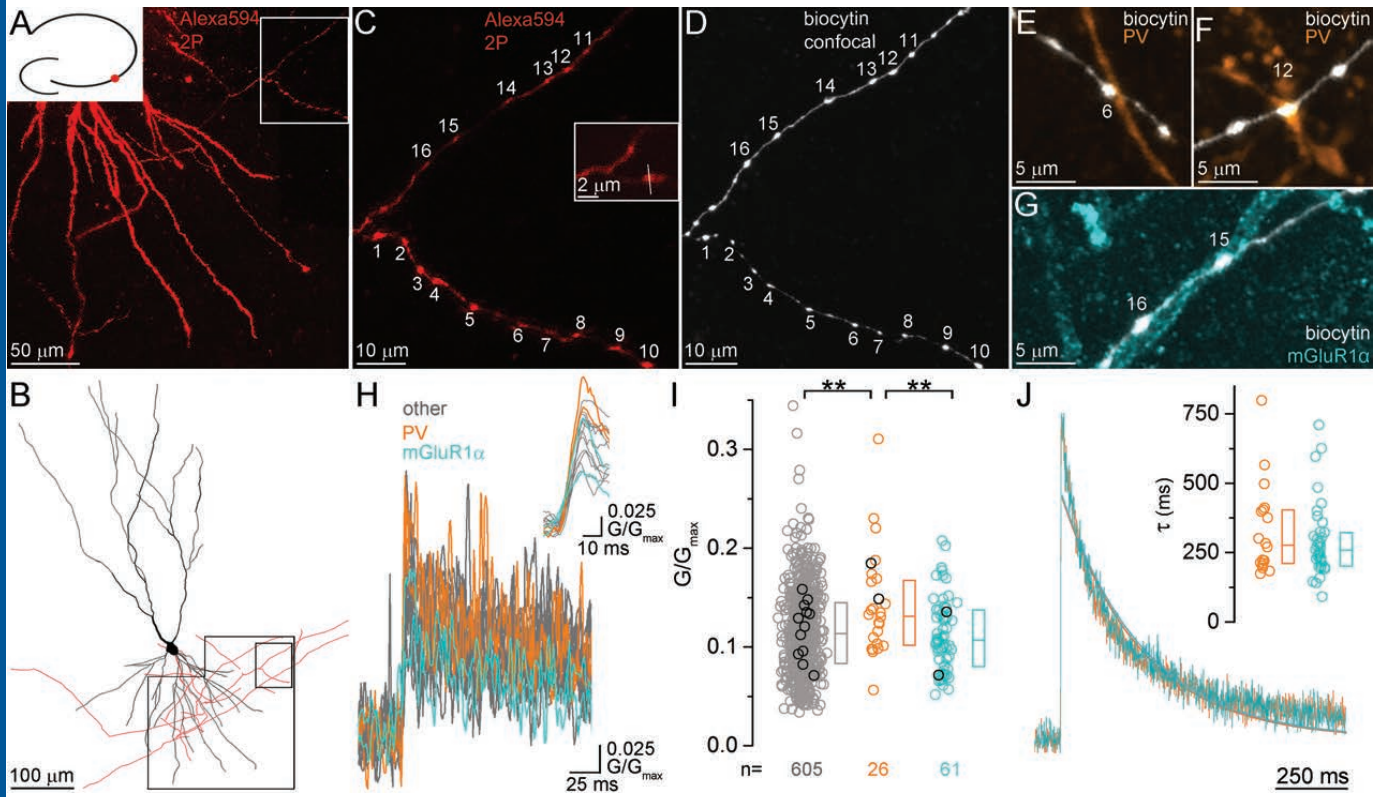
944

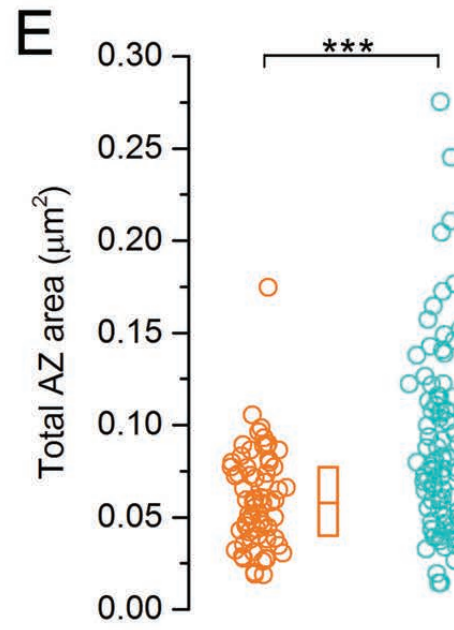
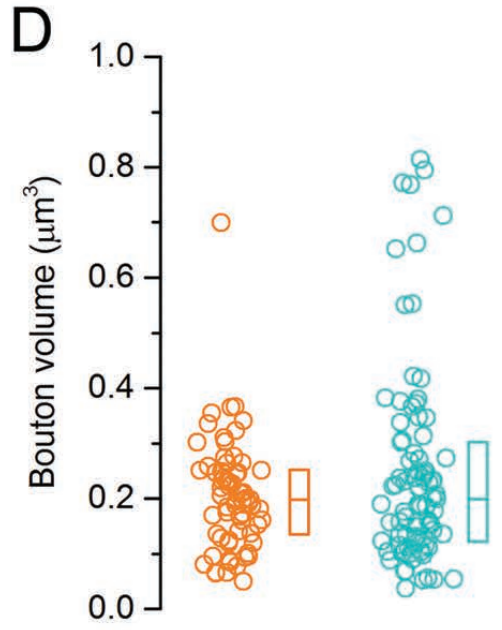
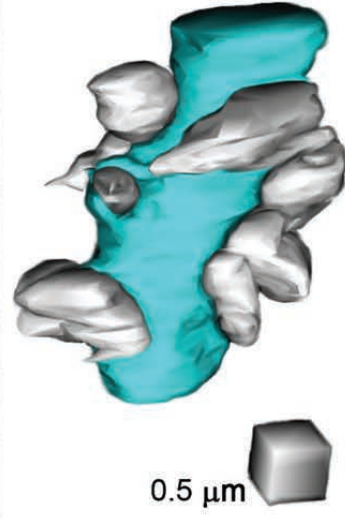
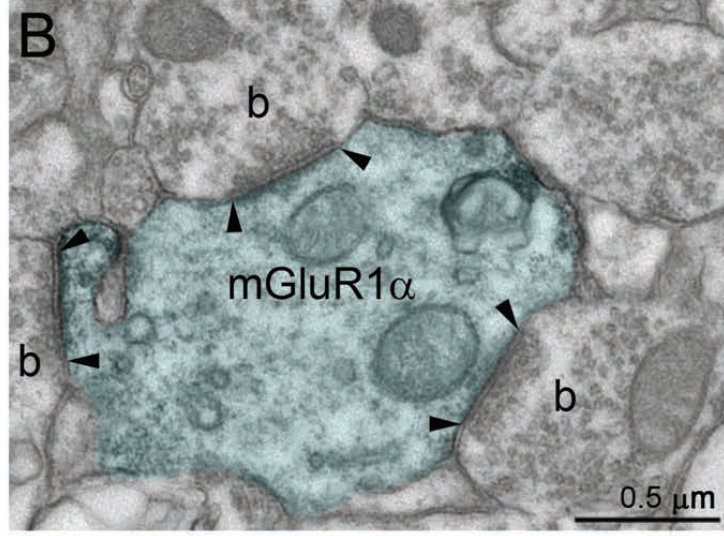
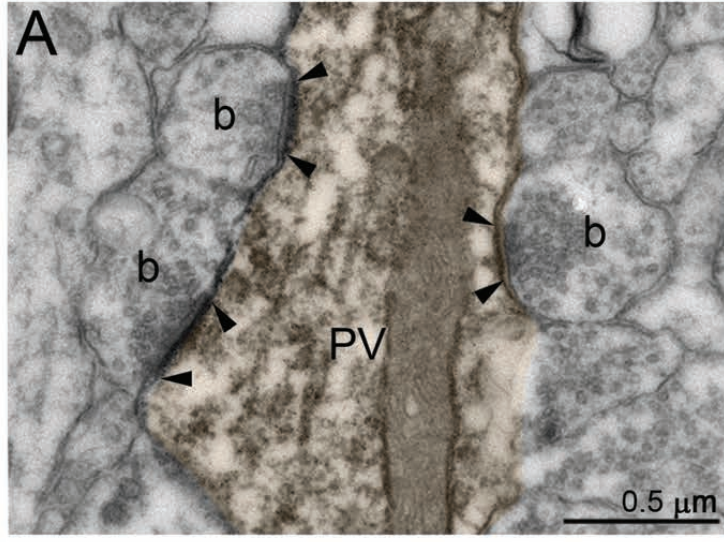
945 **Figure 6.** The densities of Cav2.2 subunit in AZs of PC boutons targeting Kv3.1b⁺ and
 946 mGluR1 α ⁺ dendrites. **A, B**, A Kv3.1b⁺ dendrite (dendrite_{PF} in **A**) is contacted by boutons
 947 whose PF (b_{PF}) membranes show strong Cav2.2 subunit reactivity in their AZs (orange in **B**).

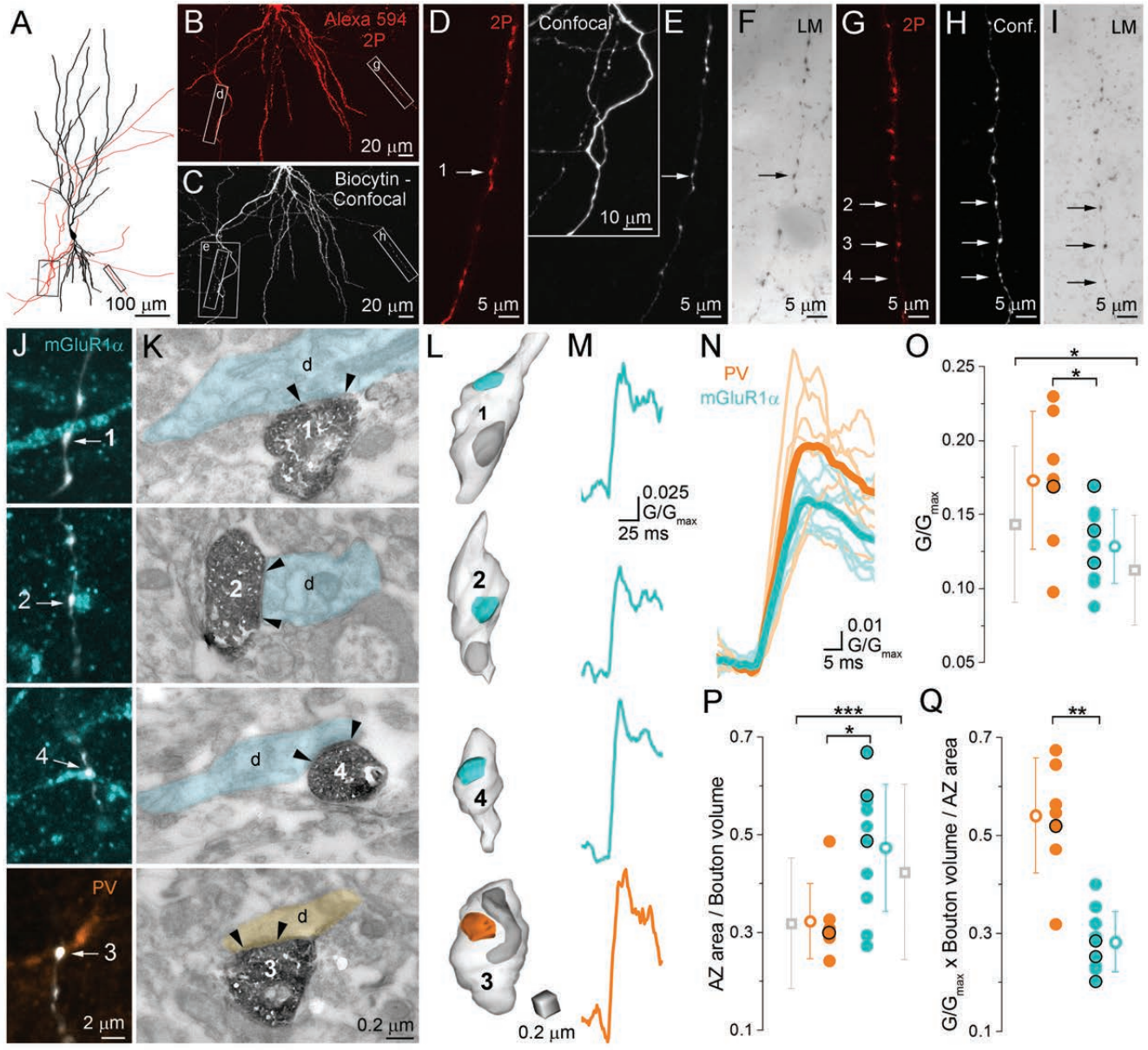
948 **C, D**, High magnification images of the boxed areas shown in **A, B, E, F**, PF bouton
 949 membranes contacting an mGluR1 α^+ dendrite (dendrite_{PF} in **E**) contain Cav2.2 subunit
 950 immunolabeled AZs (cyan in **F**). **G-I**, Enlarged views of the boxed areas in **E, F**. **J**,
 951 Normalized densities of gold particles labeling the Cav2.2 subunit within presynaptic AZs
 952 (syn.) and extrasynaptic membranes (extrasyn.) of boutons contacting Kv3.1b $^+$ or mGluR1 α^+
 953 profiles and in surrounding EF membranes (background: bg., grey). *Post hoc* MW U-tests
 954 with Bonferroni correction after Kruskal-Wallis test ($p < 0.0001$) demonstrated a significant
 955 difference between the synaptic and background labeling ($p < 0.0001$). Circles indicate
 956 individual measurements of AZs, the boxes represent interquartile ranges with the horizontal
 957 bars showing the medians. **K**, Comparison of \overline{NNDs} measured in 21 Kv3.1b $^+$ and 40
 958 mGluR1 α^+ dendrite-contacting AZs to their random controls (repeated 1000 times). Wilcoxon
 959 signed-rank test revealed significant difference ($p < 0.0001$) between the data and the random
 960 distributions for both AZ populations. **L**, The $\overline{g(r)}$ of individual Kv3.1b $^+$ ($n = 21$) or
 961 mGluR1 α^+ ($n = 40$) dendrite-targeting AZs is plotted against the $\overline{g(r)}$ of their random
 962 controls (repeated 1000 times). Wilcoxon signed-rank test revealed significant differences (p
 963 < 0.0001) between the data and the random distributions for both AZ populations.
 964
 965 **Figure 7**. EM tomography of the AZs of PC axon terminals synapsing onto PV $^+$ or mGluR1 α^+
 966 dendrites. **A, D**, Electron tomographic subvolumes (0.6 nm thick) of representative boutons
 967 (b) establishing asymmetric synaptic contacts (arrowheads demarcate the edges of the
 968 synapses) on a PV $^+$ (orange, **A**) and a mGluR1 α^+ (cyan, **D**) dendrite (labeled with pre-
 969 embedding peroxidase reaction). **B-C** and **E-F**, Higher magnification views show docked (**B**
 970 and **E**, area boxed on **A** and **D**, respectively) and predocked vesicles (**C, F** from the same
 971 tomographic subvolumes). **G, H**, Docked (**G**, $p = 0.01$, MW U-test) and membrane proximal
 972 (**H**, $p = 0.037$, MW U-test, docked + pre-docked vesicles) vesicles have significantly different

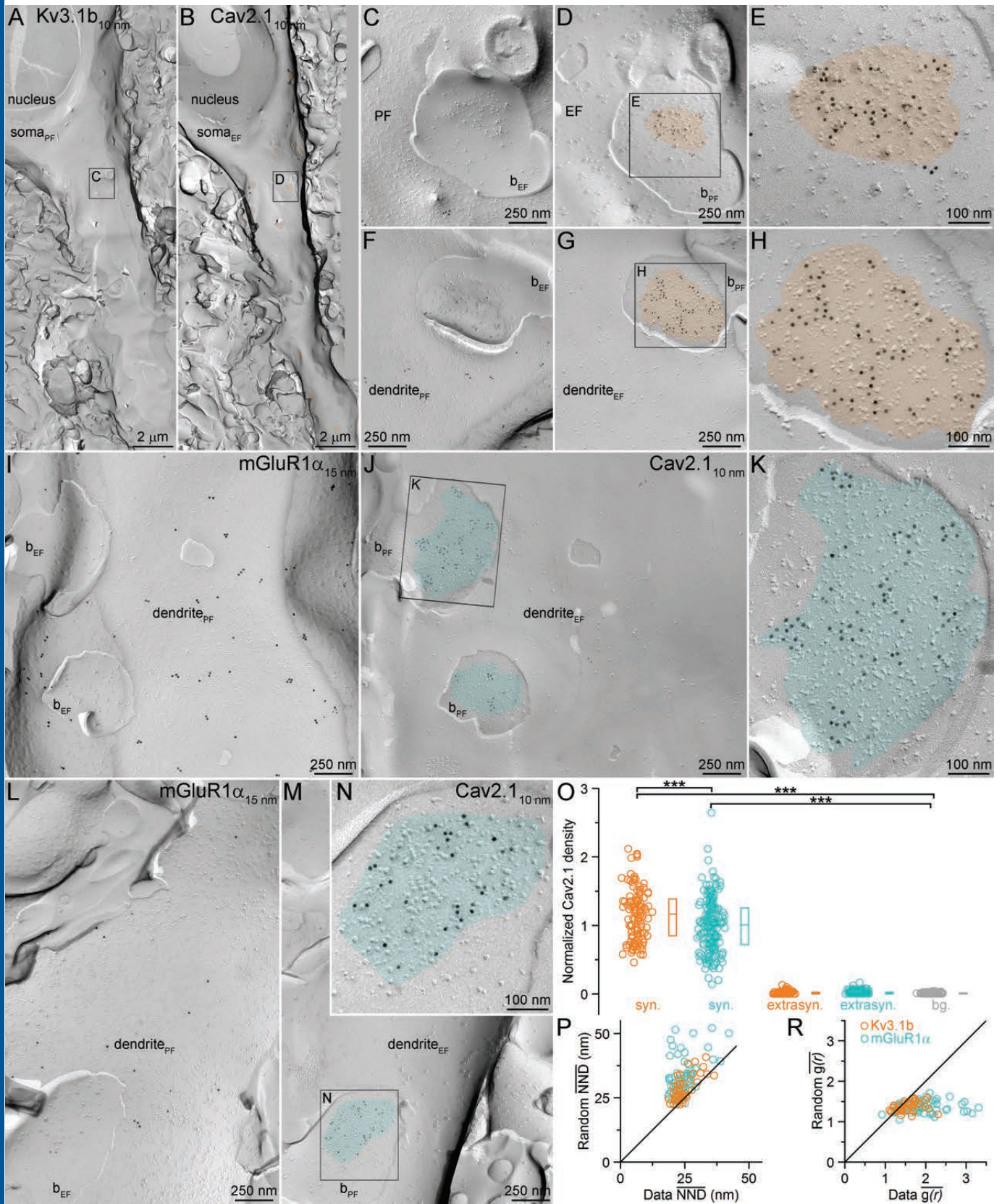
973 densities (PV^+ : $n = 47$; $mGluR1\alpha^+$: $n = 49$ subvolumes) in the two AZ populations. Circles
974 indicate individual AZ subvolumes; boxes represent interquartile ranges with the horizontal
975 bars showing the medians.

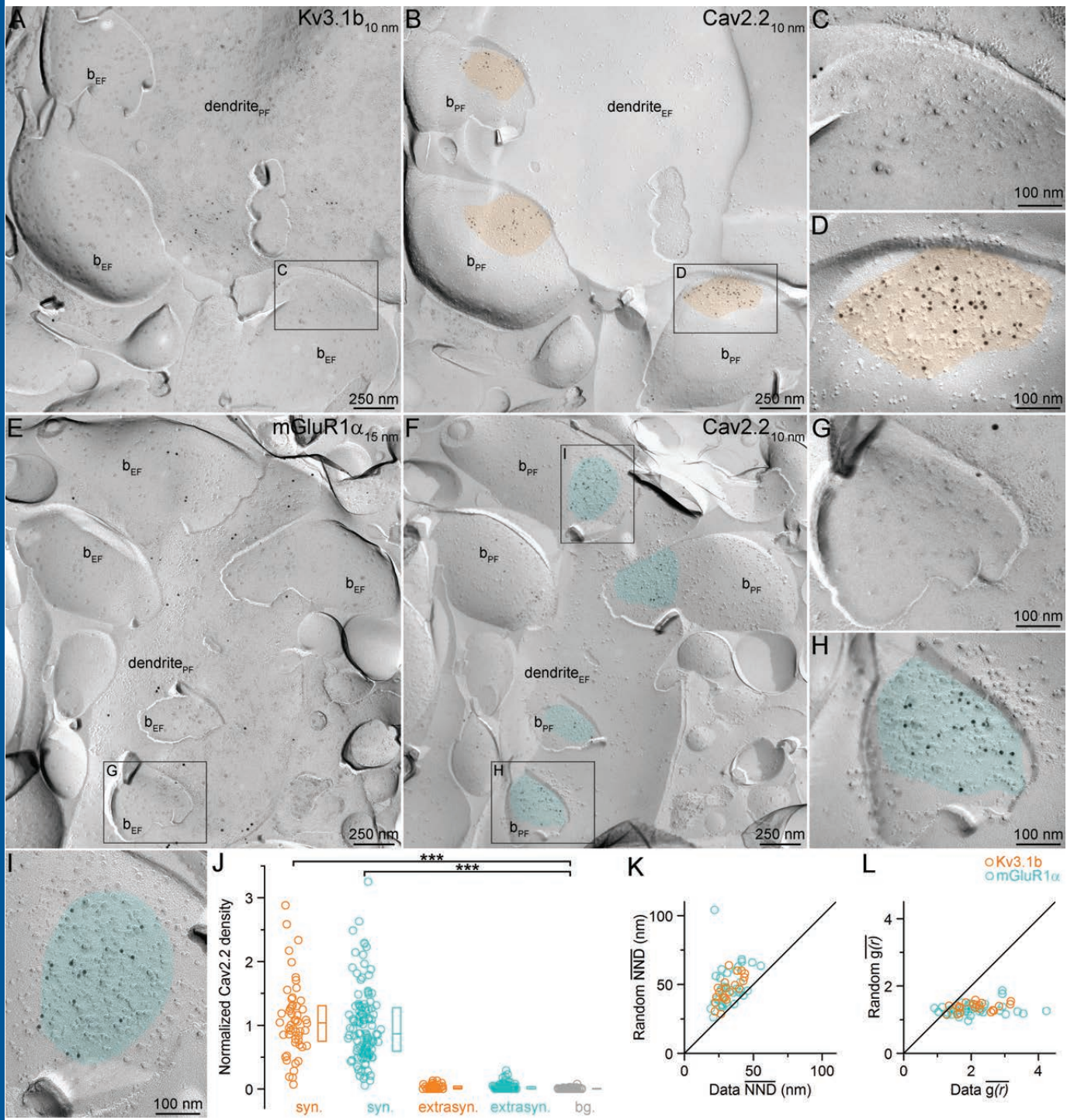


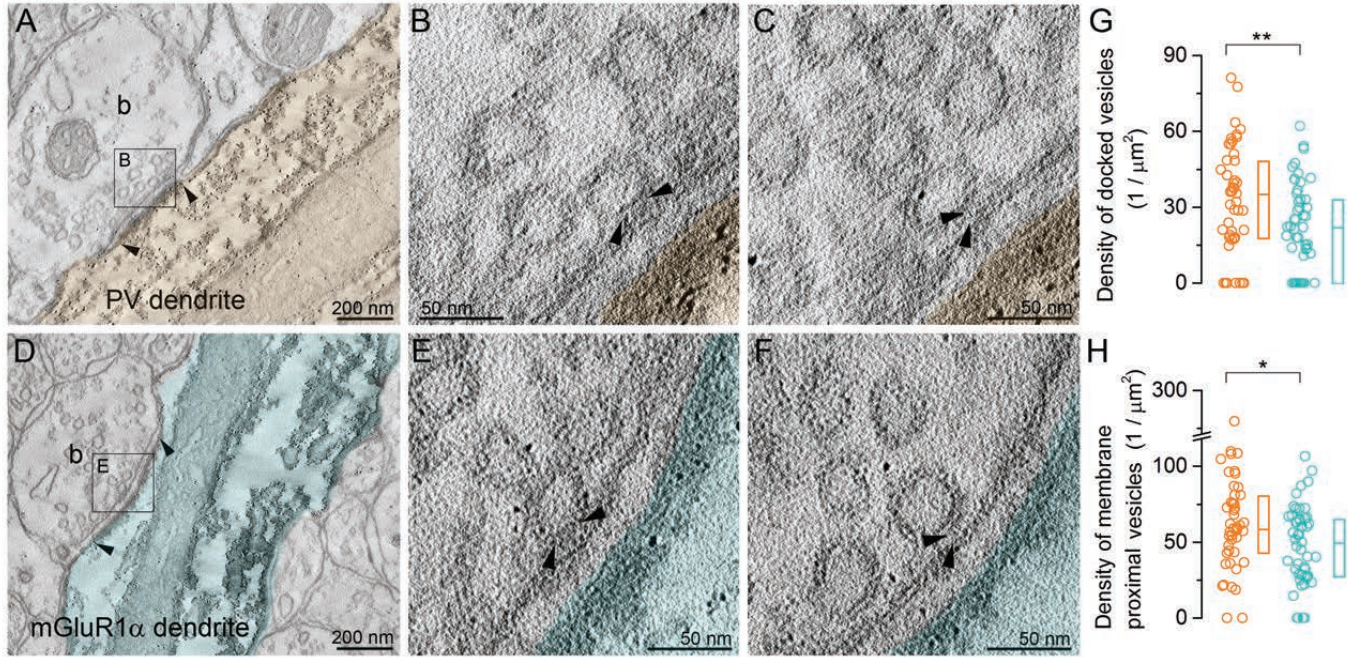












	PV ⁺ dendrite-targeting boutons					mGluR1 α ⁺ dend.-targeting boutons					Test	p
	Mean	SD	Median	n	# animal	Mean	SD	Median	n	# animal		
Peak amplitude of [Ca ²⁺] transient (300 μ M Fluo5F) (G/G _{max})	0.14	0.05	0.13	26*	15	0.11	0.04	0.11	61*	23	MW U-test	0.012
Normalized peak amplitude of [Ca ²⁺] transient (300 μ M Fluo5F) ¹	1.20	0.41	1.12	26*	15	1.00	0.28	0.98	61*	23	t-test	0.024
Peak amplitude of [Ca ²⁺] transient (100 μ M Fluo5F) (G/G _{max})	0.21	0.10	0.22	14*	9	0.17	0.11	0.14	21*	13	MW U-test	0.100
Normalized peak amplitude of [Ca ²⁺] transient (100 μ M Fluo5F) ¹	1.33	0.51	1.36	18*	12	1.04	0.25	1.03	35*	18	t-test	0.037
Bouton volume in perfused tissue (μ m ³)	0.20	0.10	0.20	67*	3	0.25	0.18	0.20	87*	3	MW U-test	0.650
Bouton volume <i>in vitro</i> slices (μ m ³)	0.31	0.12	0.26	7	5	0.20	0.12	0.18	10	4		
Total AZ area in perfused tissue (μ m ²)	0.06	0.03	0.06	67*	3	0.09	0.05	0.08	87*	3	MW U-test	0.000
AZ area <i>in vitro</i> slices (μ m ²)	0.10	0.04	0.09	7	5	0.09	0.03	0.09	10	4		
Cav2.1 density in AZs (gold/ μ m ²) ²	373	47	370	112	5	321	46	325	172	5		
Cav2.2 density in AZs (gold/ μ m ²) ²	151	30	139	52	4	130	39	130	114	4		
Cav2.1 extrasynaptic density (gold/ μ m ²) ²	2.14	2.46	2.21	93	5	2.88	2.64	2.23	174	5		
Cav2.2 extrasynaptic density (gold/ μ m ²) ²	2.69	3.15	2.35	48	4	1.02	1.26	0.75	113	4		
Background Cav2.1 density (gold/ μ m ²) ²	2.27	1.93	2.94	132	5	2.27	1.93	2.94	132	5		
Background Cav2.2 density (gold/ μ m ²) ²	0.66	0.33	0.62	104	4	0.66	0.33	0.62	104	4		
Cav2.1 NND distance (nm)	24.7	4.0	23.3	43	5	24.3	4.6	23.1	72	5		
Cav2.2 NND distance (nm)	32.1	7.2	30.3	21	4	32.0	8.3	28.7	40	4		
Docked vesicle density (vesicle/ μ m ²)	33.1	21.1	35.5	47*	3	21.9	17.5	22.2	49*	3	MW U-test	0.010
Membrane proximal vesicle density (vesicle/ μ m ²)	64.9	42.0	59.1	47*	3	47.3	26.6	49.9	49*	3	MW U-test	0.037